

Contents lists available at ScienceDirect

Chemical Geology

journal homepage: www.elsevier.com/locate/chemgeo





Accurate analyses of key petrogenetic minor and trace elements in olivine by electron microprobe

Peng Jiang a,b,*, Michael Perfit a, David A. Foster a, Andres Trucco c

^a Department of Geological Sciences, University of Florida, Gainesville, FL 32611, USA ^b Department of Earth Sciences, University of Hawai'i at Manoa, HI 96822, USA ^{- c} Herbert Wertheim College of Engineering-Research Service Centers, University of Florida, Gainesville, FL 32611, USA

ARTICLEINFO

Editor: Dr. Balz Kamber

Keywords: HP-EPMA
Accurate EPMA trace element analysis
Olivine geochemistry
Mantle source lithologies
Magma differentiation
East Pacific Rise

ABSTRACT

Abundances of minor and trace elements in olivine are increasingly used as petrogenetic indicators for mantle source lithologies, mantle metasomatism history, mantle potential temperatures, and magmatic differentiation. As it is common for olivine to be complexly zoned on a fine-scale, high precision analytical methods for EPMA (electron microprobe microanalyzer, or Electron Microprobe) trace element analysis under high spatial resolution have been developed. However, previous studies have focused more on analytical precision with fewer efforts in examining the accuracy of the data. In this study, we used the Cameca SXFive field emission (FE) EPMA to fully evaluate the effects of beam settings, background offsets and background regression models, and primary calibration standards on the data accuracy of 10 key petrogenetic elements (Na, Al, P, Ca, Ti, Cr. Mn. Co. Ni. and Zn) using MongOlSh11-2 olivine as a reference material. Our results indicate that high voltage, high beam current and long counting time not only improve data precision, but also improve data accuracy, especially on elements with low P/B (peak/background) ratios such as Zn and Cr. Importantly, careful background offsets and background regression models need to be obtained via high resolution WDS relative scans or step scans on each target element. Special care needs to be paid to Co element analysis to avoid or correct for peak interference of Fe KB. Among 10 minor and trace elements, exponential background regression models need to be applied to Al, Mn, and Ti elements, whereas other elements require linear background regression. Furthermore, to avoid Al and Zn surface contamination due to alumina polishing or brass presence, ultrasonic cleaning between each intermediate polishing steps and plasma cleaning immediately prior to EPMA experiments is highly recommended. Micro-inclusions such as chromite and spinel in olivine or adjacent Ca-rich phases need to be avoided to minimize primary or secondary fluorescence-related contamination on Al, Cr, or Ca. As a volatile element, Na element needs to be analyzed first with appropriate counting time to minimize the Na loss under high beam conditions. It needs mentioning that major elements (Mg, Fe, and Si) are best analyzed using MongOlSh11-2 or San Carlos olivine as primary standards for calibrations, which can yield more accurate data for both major elements and trace elements because of the improved matrixcorrections. Using our recommended analytical protocols, we have successfully discriminated "depleted" mantle olivine cores from an EMORB in northern East Pacific Rise (EPR) via Ca, Ti, Ni, Co, and Mn abundances. Our olivine data from Siqueiros Transform and the nearby 8°20' N seamounts also help reveal a metasomatized peridotite mantle beneath the northern EPR. Overall, the protocols proposed in this study can serve as a guide for accurate EPMA olivine trace element analyses, which potentially contributes to the efforts of fostering a comparable olivine database worldwide.

1. Introduction magmatic differentiation (Foley et al., 2013). Minor and trace element abundances in olivine have recently been used to determine mantle
As a major mineral component in Earth's mantle and in most cases source heterogeneity, mantle metasomatic history, crustal recycling, the first silicate mineral to crystallize from mantle-derived primary mantle-crust interaction, and complex magmatic recharge, mixing and melts, olivine shows great potential in tracing mantle composition and fractional crystallization processes (e.g., Sanfilippo et al., 2014; de

^{*} Corresponding author at: Department of Geological Sciences, University of Florida, Gainesville, FL 32611, USA. E-mail address:

Received 29 July 2022; Received in revised form 30 October 2022; Accepted 1 November 2022 Available online 5 November 2022

0009-2541/© 2022 Elsevier B.V. All rights reserved.

Maisonneuve et al., 2016: Neave et al., 2018: Jankovics et al., 2019: Rasmussen et al., 2020; Liu et al., 2021; Shi et al., 2022). Among the minor and trace elements in olivine, Na, Al, P, Ca, Ti, Cr, Mn, Co, Ni, and Zn commonly have concentrations over 10 ppm that can be analyzed by electron probe microanalyzer (EPMA) (Batanova et al., 2015). Concentrations of Al, Cr, Ca, and Na are proposed to be dependent on temperature (and/or pressure), and can serve as good geothermobarometers (Wan et al., 2008; De Hoog et al., 2010; Coogan et al., 2014; Su et al., 2019). Ca and Ti show potential for discriminating "mantle" olivines from "igneous" olivines and tracing chemistry of metasomatic melts (Foley et al., 2013). Mn/Fe and Zn/Fe ratios have been used to constrain mantle source lithologies because they do not significantly fractionate during melting or olivine crystallization (Sobolev et al., 2007; Le Roux et al., 2011). Furthermore, Ni and Co show strong correlation with crystallization (Rasmussen et al., 2020; Wang et al., 2021) and P, Al, Cr are relatively slow-diffusing elements suitable for preserving complicated magmatic histories and determining timescales of magmatic processes (de Maisonneuve et al., 2016; Gordeychik et al., 2018; Shea et al., 2019; Costa et al., 2020; Yang et al., 2021).

The significant applications of the 10 minor and trace elements in olivine mentioned above demand accurate data acquisition. Compared to the commonly employed laser ablation inductively coupled plasma spectrometry (LA-ICP-MS) for olivine trace element analyses, EPMA shows its advantage by 1) having exceptionally high spatial resolution at micron scale, 2) the capability of acquiring major, minor and trace elements in one single analysis, and 3) generating useful compositional X- ray maps and/or backscattered electron (BSE) images to guide fine-scale analysis. Research indicates that accurate olivine trace element analysis by LA-ICP-MS requires ≥100 µm spot sizes to mitigate potential downhole fractionation effects for certain elements such as Na, P, Mn, Co, Ni and Zn (Bussweiler et al., 2019), and that high Na backgrounds can be present during ICP-MS analysis (De Hoog et al., 2010). High spatial resolution is particularly important when olivine has micro-scale growth zonation or when a detailed profile analysis is required for diffusion modeling purposes (Fig. 1). Previous analytical developments by Batanova et al. (2015, 2018) have shown the capability of modern EPMA for acquiring high precision trace element concentrations in olivine by increasing voltage, beam current and counting time. Their analytical protocols have made it possible to analyze low-concentration elements such as Na, P, Zn and Ti, which were not previously analyzed in the protocols developed by Sobolev et al. (2007). Furthermore, their method has been widely applied by researchers worldwide, with sometimes minor modifications of beam settings (voltage, beam current, counting time, etc.) to account for specific applications (e.g., Shaikh et al., 2019; Su et al., 2019; Zhang et al., 2022). Nevertheless, these studies focused on the precision of analyses, and did not fully discuss the details of accurate

acquisition for each element: some studies evaluated the accuracy of the analyzed elements by comparing data using different methods (such as EPMA and LA-ICP-MS) (Batanova et al., 2015, 2019; Su et al., 2019), but only a few elements such as Ti and Al have been specifically discussed for the protocols of accurate analyses (see Batanova et al., 2018). As noted by Llovet et al. (2021), there is generally an underdeveloped appreciation of the importance of fully documenting experimental conditions in publications and reporting quality control checks. To this end, we hope to address in detail the accurate acquisition of all the 10 minor and trace elements in olivine by EPMA.

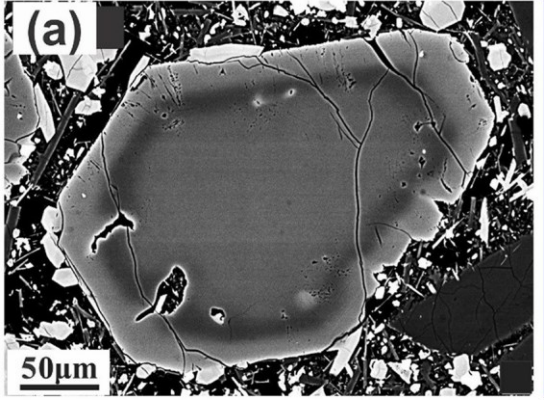
In this study, we performed experiments documenting the effects of voltage, beam size, counting time, background offsets, background regression models, and calibration standards on the accuracy of measurement of each element using the MongOlSh11–2 olivine reference material (RM) (Batanova et al., 2019). By comparing our results and reviewing published work, we discuss some pitfalls of and protocols for accurate analyses of three major elements (Mg, Fe, Si) and all 10 minor and trace elements mentioned above in olivine in order to provide helpful documentation for accurate olivine analysis. In addition to the evaluation of data accuracy, we also discuss spatial resolution, data precision, and some potential beam damage under extreme beam conditions and approaches to minimize beam damage. With our recommended analytical protocols, we have obtained geologically significant olivine data in basalts from the Siqueiros Transform and East Pacific Rise (EPR) 8'20' N seamounts.

2. Experimental design and settings

A total of 14 analytical experimental sessions on the new MongOlSh11–2 olivine RM (Batanova et al., 2019) were performed using the Cameca SXFive field emission (FE) EPMA at the University of Florida, to test spatial resolution, data precision and accuracy by changing beam conditions and analytical protocols.

The first set of analytical sessions, "Runs" 1–10, were done in July- Aug 2020 and the second set of analytical sessions, "Runs" 11–14, were done in Feb 2021. The second set of sessions were completed six months after the first set of sessions and serve to test the reproducibility of the obtained data. Each run in these analytical sessions represent a round of analysis under specified beam conditions, calibration and quantification settings, etc. A brief description of the details of each run is presented in Table 1.

Detailed wavelength dispersive spectroscopy (WDS) step scans and/ or high resolution WDS relative scans were made to best reveal the X-ray continuum for each element, so as to determine appropriate background offsets and background regression models (linear, exponential, etc.) based on the curvature of the scans. The WDS scan settings and raw data



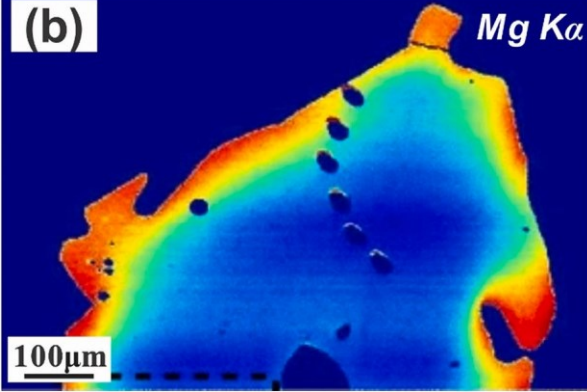


Fig. 1. The BSE image and X-ray map of olivine crystals revealing internal growth and chemical zonation. (a) BSE image of an olivine with multiple (reverse to normal) growth zones (from Jankovics et al., 2019). (b) X-ray map of Mg in olivine revealing fine-scale reverse zonation, with the potential for diffusion modeling (from de Maisonneuve et al., 2016).

Table 1
Experimental settings and key outcomes for Runs 1–14.

Runs (dates)	Beam conditions	Descriptions of analytical protocols or changes	Key outcomes					
Run 1 (2020-7-31)	15 kV, ~530 nA	Analysis on Grain 01 (EPMA mount), see Tables 51.1 and 52.1 for analytical protocol (calibration and quantification) details.	Overall consistent with reference values within errors. P, Ti, Co, and Zn show larger deviations.					
Run 2 (2020-8-3)	15 kV, ~530 nA	A focused beam changed to a defocused beam with 5 μm in size. Other settings remain unchanged.	No observable change.					
Run 3 (2020-8-3)	15 kV, ~530 nA	Co, Zn, Na, P background offsets adjusted, Ti regression method changed to "linear"; peak counting time shorten, see Table S2.2	Co data improved; Ti data turned negative; No notable improvements on Na, P, and Zn.					
Run 4 (2020-8-3)	15 kV, ~530 nA	Zn background offsets switched back as in Run 1; Ti regression method back to "exponential"; all other settings same as in Run 3.	All elements show great consistence with references, expect for Zn (still overestimated).					
Run 5 (2020-8-4)	15 kV, ~530 nA	Same settings as Run 4, but the Grain 02 (EPMA mount).	Notable Na and Al (in particular) overestimation.					
Run 6 (2020-8-4)	15 kV, ~530 nA	Mn background offsets changed (Table S2.2), other settings same as Run 4; Analysis on Grain 01.	Na and Al data back to normal; No observable improvements for Mn.					
Run 7 (2020-8-12)	25 kV, ~530 nA	New calibration (Table S1.2) and quantification (Table S2.3) under 25 kV; Background offsets of Si, Ca, and Ni adjusted (Table S2.2); Ca regression changed to "exponential"; analysis done on Grain 01.	Data overall consistent with data obtained under 15 kV; Ca slightly overestimated while Ni, Si, and Zn data accuracy improved.					
Run 8 (2020-8-12)	25 kV, ~530 nA	Same settings as Run 7, but on a MongOlSh11–2 olivine grain in the LA mount.	Notable Na and Al (in particular) overestimation again (same as Run 5).					
Run 9 (2020-8-12)	25 kV, ~530 nA	Same settings as Run 7, with a newly added Sc element (Table S2.3); analysis done on Grain 01 (same below).	Data very consistent with those obtained under 15 kV; Sc data not accurate.					
Run 10 (2020-8-13)	25 kV, ~530 nA	Same settings as Run 9, but with shortened total counting time (Table S2.3).	Consistent data with previous runs.					
Runs 11–14 (2021-2- 24–26)	15 kV, ~530 nA	New calibration on Mg, Fe, and Si using MongOISh11–2 as primary standard (Table S1.3). Settings same as Run 7, but with Ca regression as "linear" and shortened total counting time (Table S2.4).	Significant improvements of major elements (Mg, Fe, and Si) data accuracy.					

are presented in Tables X1 and X2. WDS scans with recommended background offsets and background regression models are presented in Fig. 2. Calibration standards, spectrometers (SP1-SP4), crystals (LiF, LLiF, TAP, LPET), background regression methods and offsets, and beam settings for 14 runs on Mg, Fe, Si (major elements) and Na, Al, P, Ca, Ti, Cr, Mn, Co, Ni, and Zn (minor and trace elements) are listed in Table S1. The quantification settings for 14 runs are listed in Table S2 and the recommended quantification settings with key outcomes (detection limits, precision, and accuracy) for representative runs (Runs 4, 10, 11–14) are provided in Table 2.

3. Spatial resolution of EPMA olivine analyses: Micron-submicron scale

High spatial resolution is a key aspect of EPMA analysis, helping to reveal complex mineral growth history recorded in micro-scale chemical variations. The X-ray emission volume is a radially distributed volume generated by the emitted X-rays that are closely related to the accelerating potential. However, the applied beam diameters (from 100 nm to a few microns) also affect the final emission volume. Jercinovic et al. (2008) proposed that the effective analytical resolution (AR) can be expressed as $DAR = (D^2beam + D^2emission)^{1/2}$, where Dbeam is the beam diameter and Demission is the diameter of the emission volume. To best estimate the spatial resolution under different beam conditions, we used the CASINO software (Drouin et al., 2007) to model electron energy distributions (Fig. 3). In the models, we applied an average olivine density of 3.25 g/cm³ with a composition of (Mg, Fe)₂SiO₄, and a 15 nm carbon coat on the top. A total of 10,000 electron trajectories in each Monte Carlo simulation were made to model the interactive volume under 10 kV, 15 kV, 25 kV, with a focused (100 nm) or defocused beam (5 µm). As is shown in Fig. 3, with a focused beam, the spatial resolution can be down to sub-micron scale (0.8-1 μ m) under 10 kV (Fig. 3a) and is <5 μ m under either 15 kV or 25 kV (Fig. 3b-c). With a defocused beam at 5 μm under 25 kV, the horizontal spatial resolution drops to 8-9 µm while the vertical resolution remains unchanged (3-4 μm) (Fig. 3d). It needs mentioning that the sub-micron scale spatial resolution can be theoretically reached under 10 kV (or lower), but this relatively low voltage would make it harder to get high precision and low detection limits of the data.

Although olivine is a beam resistant mineral (Shea et al., 2019), extreme beam conditions may still damage the sample to some extent (Fig. 4). Beam damage can be better revealed by secondary electron (SE) images (Fig. 4a vs.

4d). One way to reduce the beam damage and contamination is to apply a different coating material (such as iridium, Johnson et al., 2019). Another way is to apply the sub-counting method (e.g., Jercinovic et al., 2012; Hazarika et al., 2017; Kone čný et al., 2018; Hrushikesh et al., 2020), that is, dividing a long-period single spot analysis, e.g., >10 mins, into several cycles of shorter peak and background counting. Therefore, in cases where 5-10 μm is the required spatial resolution, 15 kV or 25 kV can be applied with a defocused beam to minimize the beam damage. In cases where <5 μm spatial resolution is required, a focused beam is needed, and a sub-counting method can be applied.

4. Data precision and reproducibility of EPMA olivine analyses

High data precision and low detection limit is a key part for EPMA olivine minor and trace element analyses, especially for those elements at low-concentration levels such as Na, P, Zn, Ti, Co, and Cr (Fig. 2, elements with weak or non-observable peaks). As is shown in the study by Batanova et al. (2018), the detection limit of an element is positively correlated with the analytical precision (standard deviation). That is, lower detection limits mean smaller standard deviations, and thus higher data precision. To improve the data precision, extreme beam conditions can be applied, such as 25 kV, 900 nA, and long peak counting time from 80 s up to 300 s (e.g., Batanova et al., 2015, 2018; Gomez-Ulla et al., 2017'; Su et al., 2019). In the 14 runs (Section 2), we used different voltages, beam sizes, and counting times with a constant beam current at ~530 nA. Under 15 kV, ~530 nA, and peak counting time from 120 s to 240 s, the detection limits are 20 ppm for Na, 10 ppm for Al, 15 ppm for P.

16 ppm for Ti, 55 ppm for Cr, 29 ppm for Mn, 61 ppm for Co, 38 ppm for Ni, 62 ppm for Zn, and 13 ppm for Ca, independent of beam sizes (i.e., Runs 1–2, Table S2.1, Table S4). The total analysis time is 16m10s per point. These detection limits are low enough to ensure the significance of the data: most elements (except Cr, Co, and Zn) have concentrations 3 times higher than their detection limits. With more extreme beam conditions but shorter peak counting time, i.e., under 25 kV, ~530 nA, and 60 s to 120 s peak counting, the detection limits are 24 ppm for Na, 15 ppm for Al, 19 ppm for P, 8 ppm for Ti, 26 ppm for Cr, 18 ppm for Mn, 35 ppm for Co, 19 ppm for Ni, 18 ppm for Zn, and 11 ppm for Ca (Runs 7–8, Table S2.3, Table S4), comparable to the routine detection limits range (~5–25 ppm) reported in the literature (Llovet et al., 2020). This setup has a shorter total analysis time of 12m50s. It is expected that detection limits can further decrease to below 10 ppm when 900 nA and > 240 s peak counting time are applied. However, severe beam damage may occur when operating under these extreme beam conditions for long time periods (e.g., Jercinovic et

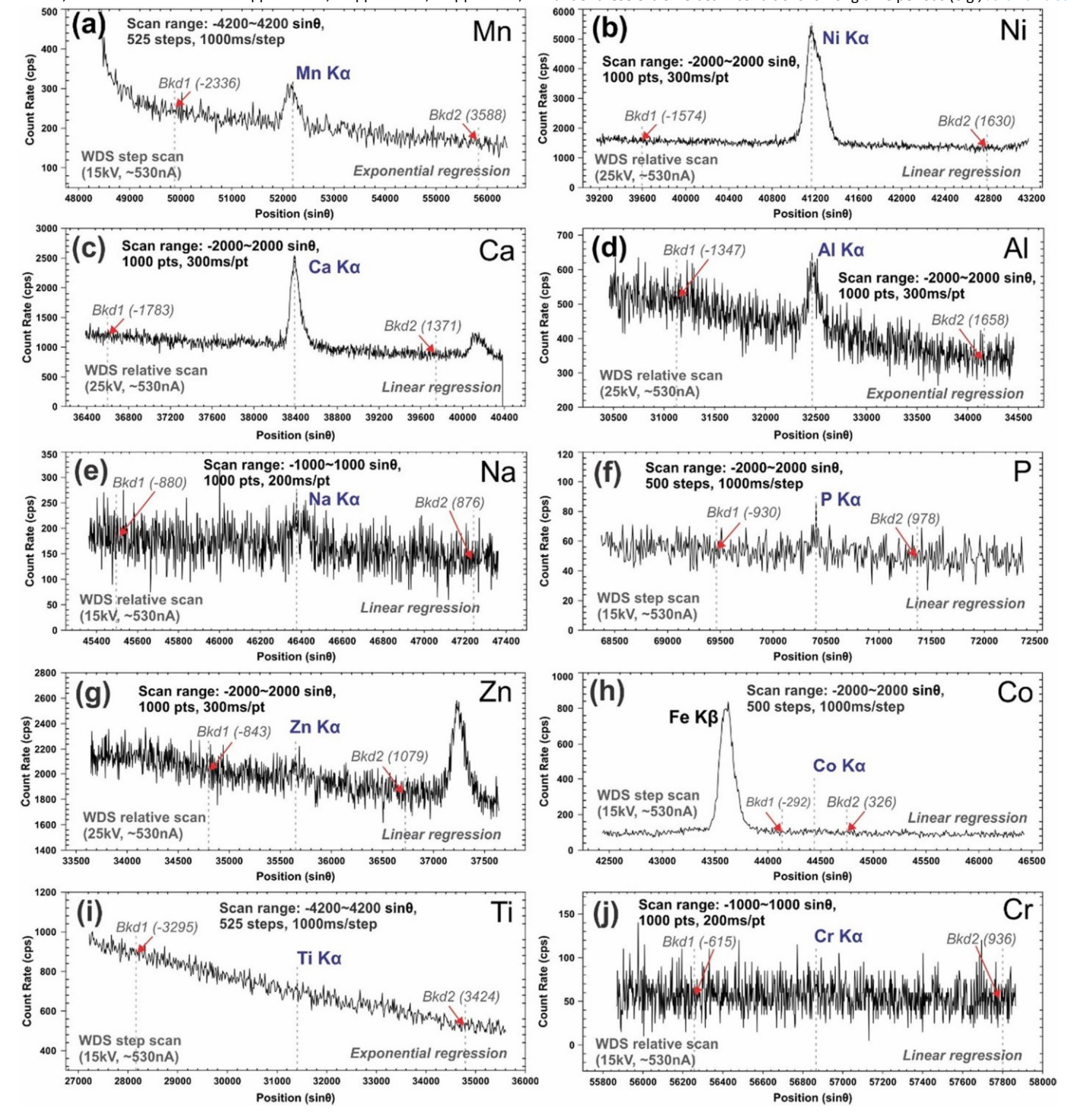


Fig. 2. (a)-(j) WDS step and relative scans for 10 minor and trace elements in MongOlSh11–2 olivine RM with recommended background offsets and background regression models illustrated. Among these elements, Ni, Ca, Al elements show notable WDS peaks (a-d), whereas Na, P and Zn show slight peaks (e-g); the other elements do not reveal observable peaks (h-j). Detailed scan settings can be referred to Table X1.

al., 2008, 2012); and the analysis would be less time-efficient. Therefore, analysts need to set appropriate beam settings for efficient EPMA analysis with sufficient data precision that meet the scientific goals. A summary of the analytical precision and detection limits in representative runs (along with recommended quantification settings) are presented in Table 2.

Recommended quantification settings and the key outcomes (detection limits, precision, and accuracy) of analyses in representative runs.

	Over t	ne 14	runs	on N	Иong	OlSh1
Representative runs	Runs 11–14 Runs 11–14 Runs 11–14	Run 4 (10) Run 4 (10)	Run 4 (10) Run 4 (10)	Run 4 (10) Run 4 (10)	Run 4 (10) Run 4 (10)	Run 4 (10) Run 4 (10)
Accuracy (dev % ***)	0.5-0.9 1.5-3.8 0.3-1.7	6 (11) ^b 3 (2)	13 (16) 5 (3)	5 (18) 14 (2)	6 (4) 6 (6)	2 (1) 75 (14)
Precision (2 stdev**)	0.2-0.3 0.2-0.4 0.1-1.6	3 (20) ^b 12 (12)	10 (15) 3 (12)	11 (10) 42 (17)	10 (21) 18 (19)	65 (25) 7 (9)
Detection limits (ppm*)	163–180 736–779 146–155	21 (29) ^b 15 (19)	22 (23) 18 (13)	16 (10) 55 (45)	41 (22) 91 (61)	55 (23) 63 (22)
Peak count time (s)	30 30 30	120 (80) ^b 120 (80)	60 (40) 60 (40)	120 (80) 120 (40)	60 (40) 120 (40)	60 (40) 120 (80)
Bkd regression methods	Linear Linear Linear	Linear Exponential	Linear Linear	Exponential Linear	Exponential Linear	Linear Linear
Bkd offsets	$-1650 \sim +1171$ $-1433 \sim +1263$ $-2430 \sim +2280$	-880 - +876 -1347 - +1658	$-930 \sim +978$ $-1783 \sim +1371$	$-3295 \sim +3424$ $-615 \sim +936$	$-2336 \sim +3588$ $-292 \sim +326$	$-1574 \sim +1630$ $-843 \sim +1079$
Voltage (kV) Beam current (nA)	20 20 20	~530 ~530	~530	~530	~530	~530 ~530
Voltage (kV)	15 15 15	$15 (25)^a$ $15 (25)^a$	15 (25) ^a 15 (25) ^a	15 (25) ^a 15 (25) ^a	15 (25) ⁸ 15 (25) ⁸	15 (25) ^a 15 (25) ^a
Crystal	TAP LiF TAP	TAP TAP	LPET LPET	LPET LiF	LLiF LiF	LLiF LLiF
Standard	MongOlSh11-2 MongOlSh11-2 MongOlSh11-2	Albite Corundum	Apatite Wollastonite	Rutile Cr ₂ O ₃	Rhodonite Cobalt	Nickel Sphalerite
Element	Mg Fe Si	Na Al	Са	E 5	Mn	Ni Zn

Note: This table summarizes the recommended quantification settings (including background offsets, background regression methods) based on the observations on 14 runs. Analytical spot size can be 5 µm to reduce beam bedamage but can also be a focused beam for high spatial resolution. The voltage, beam current, and peak count time eaglested to meet specific scientific expectations. Representative runs (Runs 4, 10, 11–14) are glamage but can also be a focused beam for high spatial resolution. The voltage, beam current, and peak count time examples of the key outcomes, i.e., detection limits, precision, and accuracy of the analyses, under 15 or 25kV with varying peak counting times. The standards listed in the table are for the accultantion purposes, detailed calibration settings can be referred to Supplementary Table S1.3. The quantification settings and the changes over the 14 runs are presented in Table S2.

* Detection limits for major, minor and trace elements, all in ppm. The detection limit is calculated by the CAMECA PeakSight software at a 99.7% confidence level (3 standard deviations). ** For Mg, Fe, Si, the precision is presented as ppm. *** Deviation (%) from the accepted reference values of the MongOlSh11–2 olivine (Batanova et al., 2019). S6

at wt.% for corresponding oxides (i.e., MgO, FeO, and SiO₂); for all other elements, precision, and accuracy) used and obtained under 25 kV (i.e., Run 10).

The numbers in the bracket indicate the values (peak count time, detection limits, precision, and accuracy) used and obtained under 25 kV (i.e., Run 10).

6

background offsets and background regression models are set, the data are consistent with quoted values within errors (Figs. 6–9, Table X3), regardless of the beam size changes, peak counting time or relatively long periods of time between analyses (in a few weeks or over 6 months) (Figs. 6–9). These points support the reproducibility of the data and the reliability of the method. Elements with significant variations (such as Al, Ca, Ti, and Co) are associated with incorrect background offset selections, background regression models, or analytical procedures, which points to the focus of this paper: pitfalls and protocols for more accurate analyses (Section 5).

5. Key petrogenetic elements' data accuracy evaluation and improvements: pitfalls and protocols

To define protocols for accurate EPMA major, minor and trace analysis in olivine, we tested and evaluated the effects of voltage, beam size, counting time, background offsets, background regression models, and calibration standards over the 14 runs via measuring the international MongOlSh11-2 olivine RM (treated as "unknowns"). The details of calibration and quantification settings are presented in Table S1 and Table S2, respectively. Quantification data are presented in Table S3 (via X-PHI matrix correction method) and Table S4 (via PAP correction method). Both X-PHI (Merlet, 1992, 1994) and PAP (Pouchou and Pichoir, 1991) matrix corrections apply the Φ(ρz) (or Phi-Rho-Z) correction models where a X-ray depth distribution function $(\Phi(\rho z))$ is used to integrate X-rays for the whole excitation volume, generating more accurate data than the traditional ZAF correction (which integrates X-rays along the electron track). The data obtained by X-PHI and PAP corrections are consistent, with the PAP method revealing overall slightly higher accuracy (lower deviation % from the reference values) (see plots in Supplementary Table X4). Therefore, we applied the PAP method for all data presented in this study. Based on our thorough data accuracy evaluation and improvement, we present our recommended calibration and quantification settings in Table S1.3 and Table 2, respectively. Key outcomes (including accuracy evaluation) for representative runs (Runs 4, 10, 11–14) are also presented in Table 2.

Overall, higher voltage improves data precision and potentially data accuracy due to the increased peak/background (P/B) ratios (Newbury, 2002; Batanova et al., 2018), whereas beam size changes do not have observable effects on data accuracy. The data accuracy evaluation plots yield overall great consistence between measured values and the reference values (Fig. 5; Runs 4, 10). However, some elements show slight or significant variations over the 14 runs (Figs. 6-9), which are correlated with potential inaccurate background offsets, background regression model selections or inappropriate analytical protocols. In the following subsections, we will discuss the pitfall and protocols for accurate analyses for 3 major elements (Mg, Fe, Si) and all the 10 minor and trace elements (Na, Al, P, Ca, Ti, Cr, Mn, Co, Ni, and Zn). To simplify the discussion, 10 minor and trace elements are grouped by their potential petrogenetic applications, such as geothermobarometers (Na, Al, Ca, and Cr), mantle source lithology tracers (Ca, Ti, Mn, and Zn), and indicators of magma differentiation (Ni, Co, and P). Note that some elements can have multiple applications. 5.1. Major elements in olivine (Mg, Fe, and Si)

Major elements Mg, Fe, and Si provide information regarding key aspects of olivine growth history and temperatures of crystallization. The forsterite (Fo) content (Mg/(Mg + Fe)) in olivine may help discriminate primitive mantlederived melts and degrees of fractionation experienced by magmas (Foley et al., 2013). In addition, accurate analyses of Mg, Fe, and Si can help make accurate matrix corrections that improve the overall accuracy of minor and trace element concentrations in olivine.

Compared to the method by Batanova et al. (2015) where combined EDS (for Mg, Fe, Si) and WDS (for trace elements) detectors were used, we applied WDS detectors for both major and trace element analyses. In the first set of analytical sessions (Runs 1–10), hematite (Fe $_2$ O $_3$), periclase (MgO), and wollastonite (CaSiO $_3$) were selected as the primary standards for calibrations on Fe, Mg, and Si, respectively (Table S1.1, S1.2), whereas in the second set of analytical sessions (Runs 11–14), the matrix-matched MongOlSh11–2 olivine RM was used for these

P. Jiang et al. Chemical Geology 614 (2022) 121199

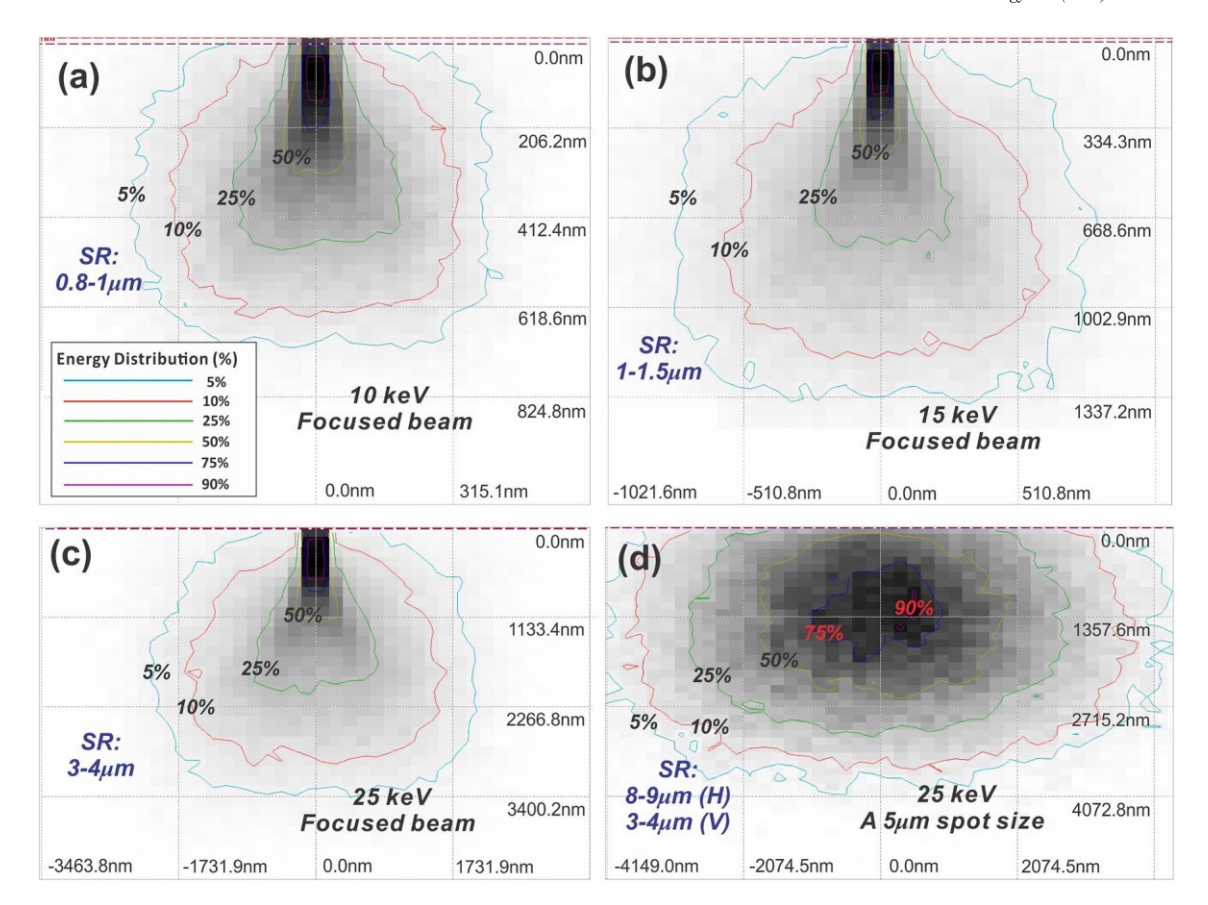


Fig. 3. (a)-(d) The Monte Carlo simulations of the electron energy distributions for olivine under 10, 15 and 25 kV, with a focused or defocused beam (5 μm). The simulations were done using the CASINO program (Drouin et al., 2007), with 10,000 electron trajectories, for each model. The 5% contour represents the distance from the beam where the majority of electrons are near 0.5 kV (under 10 kV), 0.75 kV (15 kV) or 1.25 kV (25 kV) due to the inelastic scattering in olivine. Beyond the 5% contour, X-rays are not effectively generated (thus the spatial resolution can be approximately defined by the 5% contour). With a focused beam, the spatial resolution is <5 μm under 10, 15, 25 kV. A defocused beam with 5 μm spot size can generate decreased horizontal spatial resolution to 8-9 μm with no influence on vertical resolution. SR: spatial resolution. For details of modeling parameters, see Section 3.

calibrations (Table S1.3). With this primary standard, the average compositions of Mg, Fe and Si overall yield lower deviations from the reference values, with 0.5-0.9% for Mg, 0.3-1.7% for Si, and 1.5-3.8% for Fe, compared to Runs 1-10 with 0-2.1% for Mg, 0.3-4.4% for Si, and 3.0-5.8% for Fe (see Table S4; Fig. 6ac). In addition, Runs 11-14 yield Mg, Fe and Si data with much smaller variations for each single analysis, whereas Runs 1-10 (without applying the matrix-matched MongOlSh11-2 as primary standard) reveal notable element variations or drifting, especially for Mg and Si (Fig. 6a, c). One possible cause can be the matrix difference between calibration standards and "unknown" samples. As is shown in Fig. 6d, slight shifts of the peaks and minor peaks are revealed between wollastonite (non-matrix matched Si standard) and MongOlSh11-2 (the "unknown") (Runs 1-6). After applying the wider background offsets (Runs 7-14), the drifting effect was reduced (average deviation at 1.2% for Runs 7-10 with a wollastonite standard), and was minimized when a matrix-matched standard was applied (average deviation at 0.7% for Runs 11–14; Fig. 6c). The wider background offsets are needed so as to avoid the peak interference from Si Kβ on the background acquisition (Fig. 6d). The use of a matrix-matched olivine as the primary standard, either San Carlos (Sobolev et al., 2007) or MongOlSh11-2 (Batanova et al., 2019), is highly recommended for primary calibrations on Fe, Mg and Si. Ideally, one olivine RM can be used as standard for calibration and another olivine RM can serve as "monitor standard" for data correction. In cases where such a standard is not available, careful examinations on WDS scans of both the standard and unknown samples are needed to make sure that accurate background offsets are selected separately for calibration and quantification. This approach also works for other cases where primary standards and unknown samples have

very different matrices (see Na and Al examples in Suppl. Fig. S2). 5.2. Geothermobarometers (Na, Al, Ca, and Cr)

De Hoog et al. (2010) proposed that the abundances of Na, Al, Ca, and Cr in olivine are dependent on temperature (and to some extent, pressure) in garnet peridotites, and suitable for empirical olivine thermobarometers. Among these elements, the Al-Ol and Cr-Ol thermometers are closely correlated (both dependent on Cr/(Cr + Al), i.e., the Cr#Ol), and the Al-in-olivine is the most commonly used thermometer to reveal primitive melt crystallization and mantle potential temperatures (Jennings et al., 2019; Goltz et al., 2020; Li et al., 2021). In addition, Ca in olivine also shows correlations with melt water content (geohygrometer) in subduction zone settings (Gavrilenko et al., 2016), and Na in olivine shows potential as a pressure indicator for orogenic mantle peridotite (Su et al., 2019). With these implications, accurate analyses of Na, Al, Ca, and Cr in olivine are crucial.

Analysis of Na yields overall very consistent concentrations with the reference value (cf. Batanova et al., 2019) within uncertainty (Fig. 7e). Slight changes in background offsets of Na in Runs 3–6 (Section 2, Table S2.2) do not affect data accuracy. However, when analyzing MongOlSh11–2 olivine grains in the LA mount (Run 8), the Na content is notably overestimated, which can be correlated with slight heterogeneity among different olivine grain pieces (Batanova et al., 2019). It is therefore advised to apply only one MongOlSh11–2 olivine grain (in a small area) for the purpose of "data monitoring" (as a reference material). We also noticed that, when operating under 25 kV on Grain 01

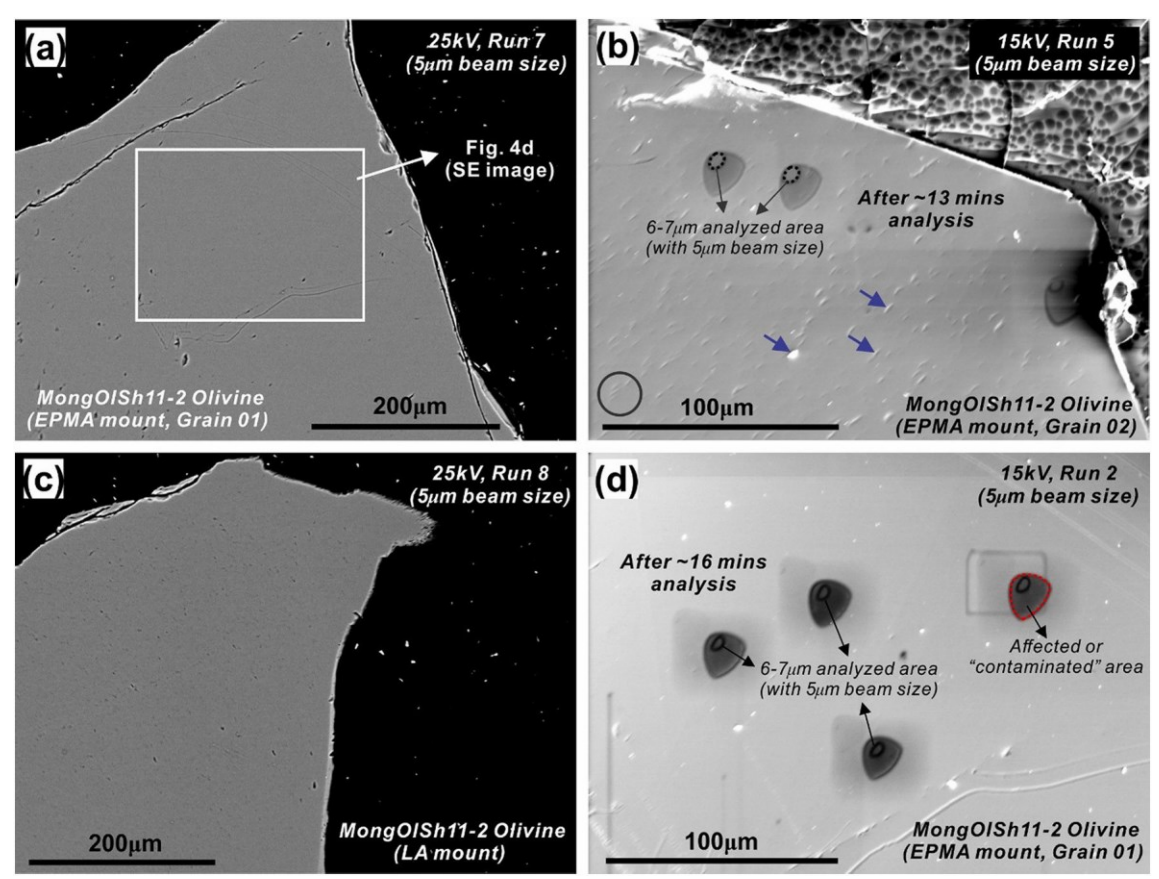


Fig. 4. BSE and SE images of the MongOlSh11–2 olivine grains illustrating the potential polishing issue and beam damage after long-time analysis under high beam conditions. (a) BSE image of Grain 01 (EPMA mount) with no observable polishing issue or beam damage. (b) SE image of Grain 02 (EPMA mount) with notable polishing holes and potential remaining polishing powders (blue arrows). The 6-7 μm analyzed area under 5 μm beam spot size corresponds to the CASINO modeled horizontal spatial resolution. (c) BSE image of a MongOlSh11–2 olivine grain in LA mount with observable polishing holes. (d) SE image of Grain 01 (a small region in Fig. 4a) showing relatively good polishing and revealing the analyzed and "contaminated" area (beam damage) under high beam conditions (15 kV, ~530 nA). (For interpretation of the references to colour in this figure legend, the reader is referred to the web version of this article.)

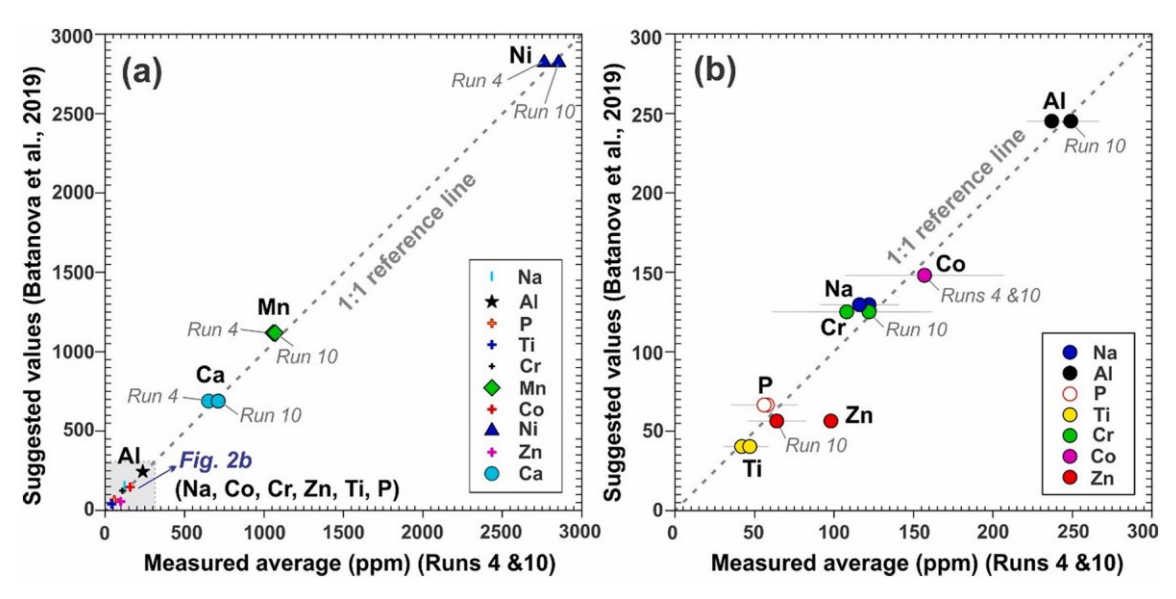


Fig. 5. (a)-(b) Data accuracy evaluation of Runs 4 and 10 for the measured 10 minor and trace elements in MongOISh11–2 olivine grains. The average compositions of each element are plotted against the reference values suggested by Batanova et al. (2019). All elements show good consistence (except for Zn, but Zn accuracy was notably improved in Run 10, under 25 kV).

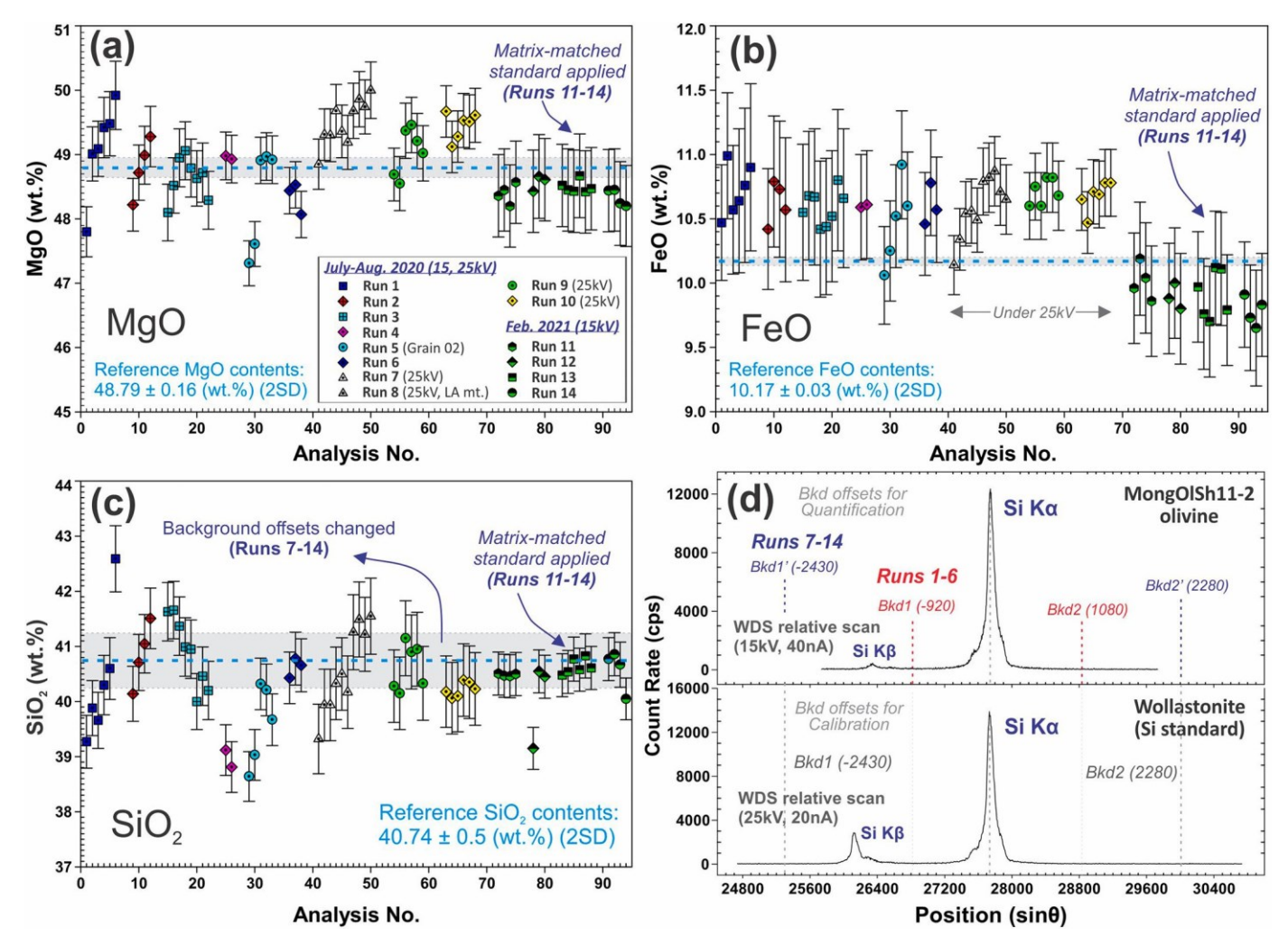


Fig. 6. (a)-(c) Accuracy evaluation on major elements (Mg, Fe, and Si) analysis using MongOlSh11–2 olivine reference material. Note that the usage of matrix- matched MongOlSh11–2 olivine as the primary standard for Mg, Fe and Si calibrations (Runs 11–14) generates more consistent Mg, Fe and Si data with reference values. (d) A comparison of the WDS scans of Wollastonite (Si standard) and MongOlSh11–2 olivine (matrix-matched Mg, Fe, Si standard). Note that slight shift of Si peak is present and that a wider range background offsets selection yields more stable Si data (with fewer fluctuations) (Runs 7–14, Fig. 6c-d). See Section 5.1 for details. The error bars in (a)-(c) reflect the analytical uncertainties for each individual analysis.

(Runs 9–10), the Na contents tend to be a little underestimated compared to previous runs (Runs 1–7). As "sodium loss" can take place under high beam current (Su et al., 2019), Na should be the first element to be analyzed among all other minor and trace elements to minimize the Na loss.

Analyses of Al yield overall high precision and high accuracy data, all falling within the reference composition range except for Run 5 and Run 8 (Fig. 7a). Abnormally high Al concentrations were obtained in Runs 5 and 8 (Fig. 7a), where the MongOlSh11-2 olivine Grain 02 (EPMA mount) and grains in LA mount were analyzed. One possible cause for this anomaly can be related to MongOlSh11-2 olivine heterogeneity in Al content (Fig. 7b), as revealed by the large Al abundance variations measured via different techniques (Batanova et al., 2019). However, considering that Al has been used as a thermometer, significant temperature variation in this reference material seems unlikely. Another possible cause for Al anomaly can be the compromised signals from spinel micro-inclusions and their corresponding secondary fluorescence (SF) Xrays (Jennings et al., 2019; Li et al., 2021). However, we have carefully avoided spinel inclusions (or adjacent spinel phases) during the analysis so this cause can be excluded as well. Here, we correlate the Al anomaly we observed with polishing-related issues: i.e., uneven polishing with potential Al₂O₃ polishing powder residuals in Grain 02 and LA mount (Fig. 4b-c). It has been reported

that Al contamination can be caused by Al_2O_3 polishing powder (Batanova et al., 2015; Nekrylov et al., 2021). Therefore, to avoid any potential contamination, it is highly recommended to apply ultrasonic cleaning during intermediate polishing steps and perform plasma cleaning (Williams et al., 2017) immediately prior to EPMA experiments. Lastly, among 14 runs, Al is one of the two elements (Al and Cr) that did not have their background offsets or background regression models changed, which supports the use of exponential background regression (Fig. 2d, Table S2.2) for accurate Al analysis, as was also suggested by Batanova et al. (2018). In addition, the polynomial background regression method was also used for Al analysis in olivine (Goltz et al., 2020).

Similar to Al, Ca analysis also yields notable overestimation in Run 8 when analyzing the LA mount (Fig. 7c). However, this overestimation is not correlated with polishing issues. Although Batanova et al. (2019) claimed that the large discrepancies of Ca contents between EPMA and ICP-MS-based methods (Fig. 7d) are related with isobaric interferences on Ca isotopes, the overestimation in both Grain 02 and LA mount (Runs 5, 8) (Fig. 7c) suggests that different olivine grains might have slight Ca content heterogeneity. Therefore, a similar analytical approach as is used with Na (i.e., limiting analyses in a small area) can be applied to avoid the heterogeneity issue. In addition, the consistently lower Ca contents in Runs 1–6 and 11–14 (both with linear background

regression but the latter has background offsets changed), and the systematically

indicated that notable Ca enhancements (100 s of ppm) can be generated when the spot analyses are 0–20 μm from the adjacent phases with ~8.5 wt% Ca

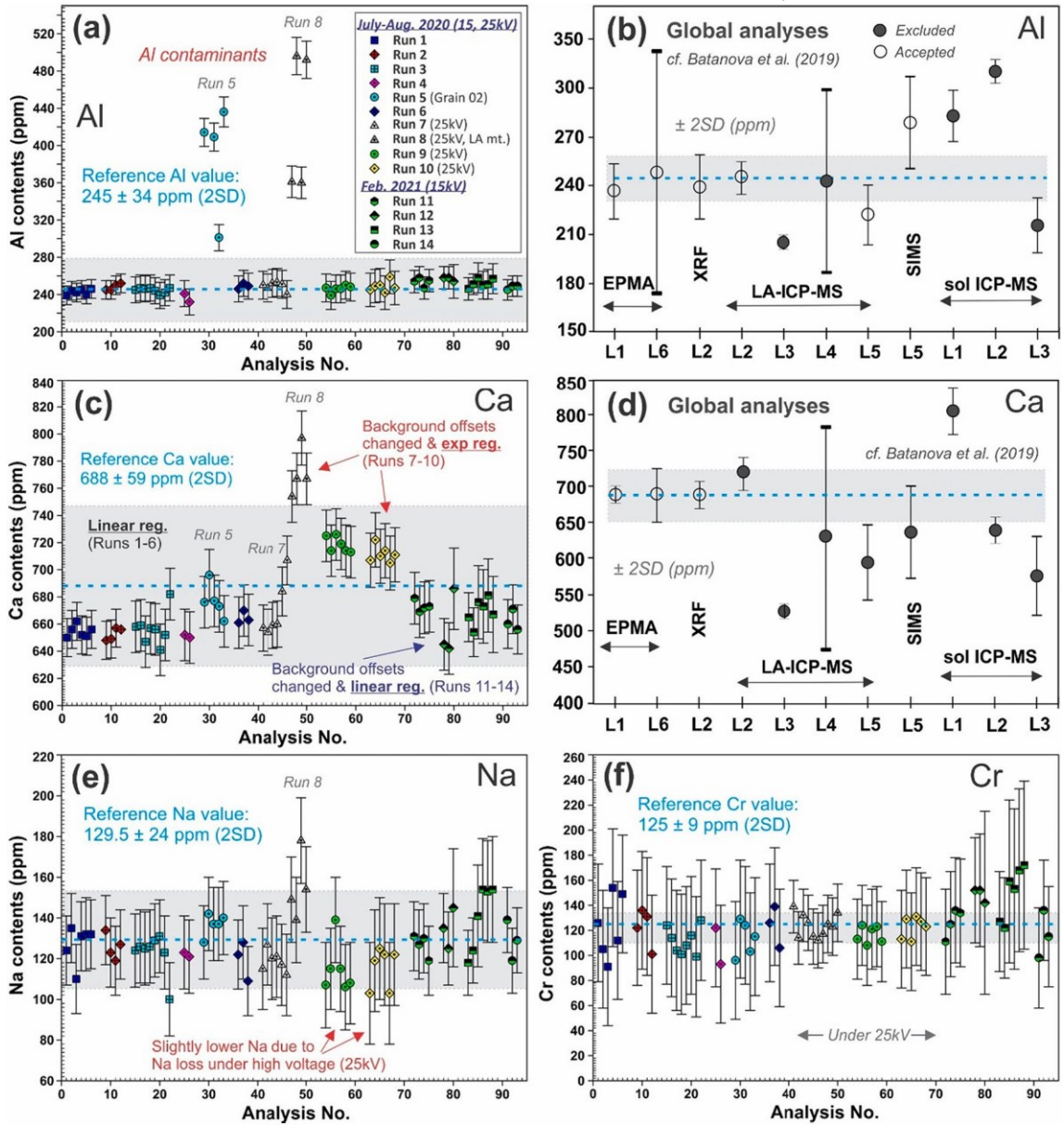


Fig. 7. Accuracy evaluation on geothermobarometers-related elements (Na, Al, Ca, and Cr) using MongOlSh11–2 olivine reference material. (a) Measured Al abundances compared to the reference value. (b) Variations of Al abundances of MongOlSh11–2 olivine using different analytical methods from different laboratories (L1-L6, see Batanova et al., 2019 for details). Notable Al overestimation in this study (Runs 5, 8) could be related with MongOlSh11–2 slight heterogeneity or polishing issues. (c)-(d) Measured Ca abundances (c, this study) and variations of Ca abundances based on different analytical methods and laboratories (d, Batanova et al., 2019). Notable increase of Ca in Runs 5 and 8 can be correlated with slight Ca heterogeneity in MongOlSh11–2 olivine RM; and the exponential background regression tends to yield overestimated Ca data (Runs 9–10 vs. Runs 11–14). (e)-(f) Measured Na and Cr abundances over the 14 runs. Note that slight Na heterogeneity is also observed (Run 8), and that higher voltage could cause notable Na loss (Runs 7, 9–10). Lower detection limits and higher accuracy of Cr analysis are observed under higher voltage (25 kV). See Section 5.2 for detailed discussion.

higher Ca contents in Runs 9–10 (on Grain 01, with background offsets changed and exponential background regression applied) suggest that changes in background offset (Table S2.2; Suppl. Fig. S1a) do not noticeably affect Ca contents, whereas the exponential background regression method yields overall higher Ca contents compared to the linear background regression. Nevertheless, all these runs (except for Run 8) yield Ca contents consistent with the reference value within uncertainty (Fig. 7c). From the above perspectives, we propose that a linear background regression is appropriate for Ca element analysis in olivine, and that a correction factor can be applied if systematic underestimation is observed. It also needs mentioning that Ca analysis in olivine needs to consider the SF effect from adjacent Ca-rich phases (such as plagioclase, pyroxene, and basaltic glass). Studies have

(Dalton and Lane, 1996; Llovet and Galan, 2003). To minimize the SF effect, analyses need to be done >50 μ m from the adjacent phases. However, in cases where olivine gains are small and a detailed profile analysis is needed, the PENEPMA program can be of help to correct the effect of SF by Monte Carlo simulations (Llovet and Salvat, 2016; Llovet et al., 2020).

Cr element analysis over 14 runs all yield data that are consistent with the reference value within errors (Fig. 7f). Similar to Al analysis, no background offsets or background regression models were changed throughout 14 runs, but it is notable that the Cr analysis under 25 kV (in Runs 7–10) yields Cr concentrations with smaller uncertainties and

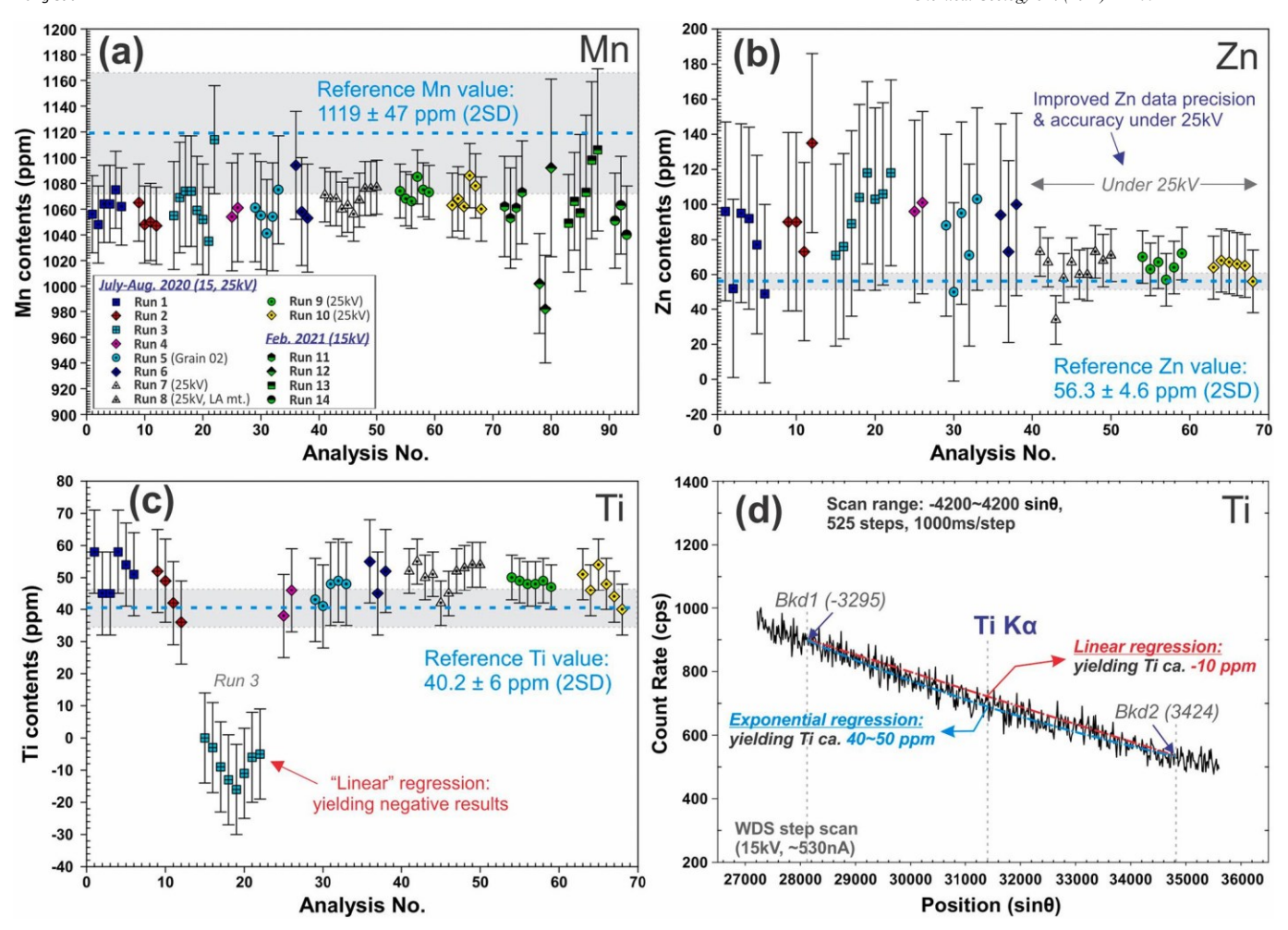


Fig. 8. Accuracy evaluation on elements (Mn, Zn, and Ti) used as mantle source lithology tracers using the MongOlSh11–2 olivine reference material. (a) Measured Mn abundances compared to the reference value. Note that Mn element analysis yields slightly underestimated values but are overall consistent with reference concentrations. (b) Measured Zn abundances compared to the reference value. Note that Zn element analysis yields more accurate concentrations when higher voltage (25 kV) was applied (Runs 7–10). (c)-(d) Measured Ti abundances compared to the reference value and a comparison of linear and exponential background regression for Ti analysis. It is noted that the linear background regression (Run 3) yields negative Ti values, and that exponential background regression yields more accurate Ti data. Note that the unstable beam current in Runs 11–14 affected the analyses of Zn and Ti so only data from Runs 1–10 are presented in the plots (Fig. 8b-c) (see Table S4 for details). The error bars in (a)-(c) reflect the analytical uncertainties for each individual analysis. higher accuracy. This supports the proposition that higher voltage can help

MongOlSh11–2 obtained by various techniques worldwide (EPMA, XRF, LA-ICP-

higher accuracy. This supports the proposition that higher voltage can help significantly improve data precision and accuracy, especially for those elements with low P/B ratios (Fig. 2 g-j). What needs mentioning again is that accurate Cr analysis in olivine also needs to avoid contamination from Cr-rich mineral inclusions (spinel, chromite, etc.) (Bussweiler et al., 2019) and the SF effects of the adjacent Cr-rich mineral phases (Llovet et al., 2020).

5.3. Mantle source lithology tracers (Ca, Ti, Mn, and Zn)

Foley et al. (2013) claimed that mantle olivines have restricted lower Ca (<700 ppm) and Ti (<70 ppm) contents, whereas igneous olivines exhibit much greater concentration ranges. Enrichments of Ca and Ti in mantle olivines provide clues of mantle metasomatism by carbonate or silicate melts (Foley et al., 2013). Regardless of whether olivines are derived directly from the mantle or formed via crystallization from mafic magmas, Mn/Fe and Zn/Fe ratios of olivines have been posited to serve as good tracers for their origins to have been related to peridotite or pyroxenite sources (e.g., Sobolev et al., 2007; Le Roux et al., 2011; Howarth and Harris, 2017). If these chemical characteristics are indicative of source lithologies, accurate analyses of Ca, Ti, Mn, and Zn in olivines are very important. As Ca has been discussed in previous subsection, only Ti, Mn and Zn will be discussed below.

Mn element analysis for all runs yield slightly underestimated values but overall are consistent with the reference concentrations within analytical uncertainty (Fig. 8a). However, when compared to the Mn variations of

MongOISh11–2 obtained by various techniques worldwide (EPMA, XRF, LA-ICP-MS, SIMS, sol ICP-MS), our measured Mn values are very consistent with those measured by LA-ICP-MS (Batanova et al., 2019). This indicates that MongOISh11–2 olivine RM might have larger Mn variations than provided. In addition to Al and Ti, Mn is another element that needs to apply the exponential background regression due to its notable WDS curvature (Fig. 2a). A change of background offsets (with a narrower range) (in Run 6, Table S2.2) does not seem to affect the data accuracy.

Analysis of Zn under 15 kV (in Runs 1–6) yields notably overestimated concentrations compared to the reference olivine value (with ~36% to ~75% deviation, Table S4) (although consistent within uncertainty) (Fig. 8b). A change of background offsets (Run 3, Table S2.2) does not help improve the data accuracy. Recent research measuring Zn suggests that the drift due to contamination by brass (e.g., the Cu–Zn sample holder) (Batanova et al., 2015) should be monitored during analysis (Trela et al., 2017; Gazel et al., 2018). However, under 25 kV (Runs 7–10), the data precision and accuracy are both significantly

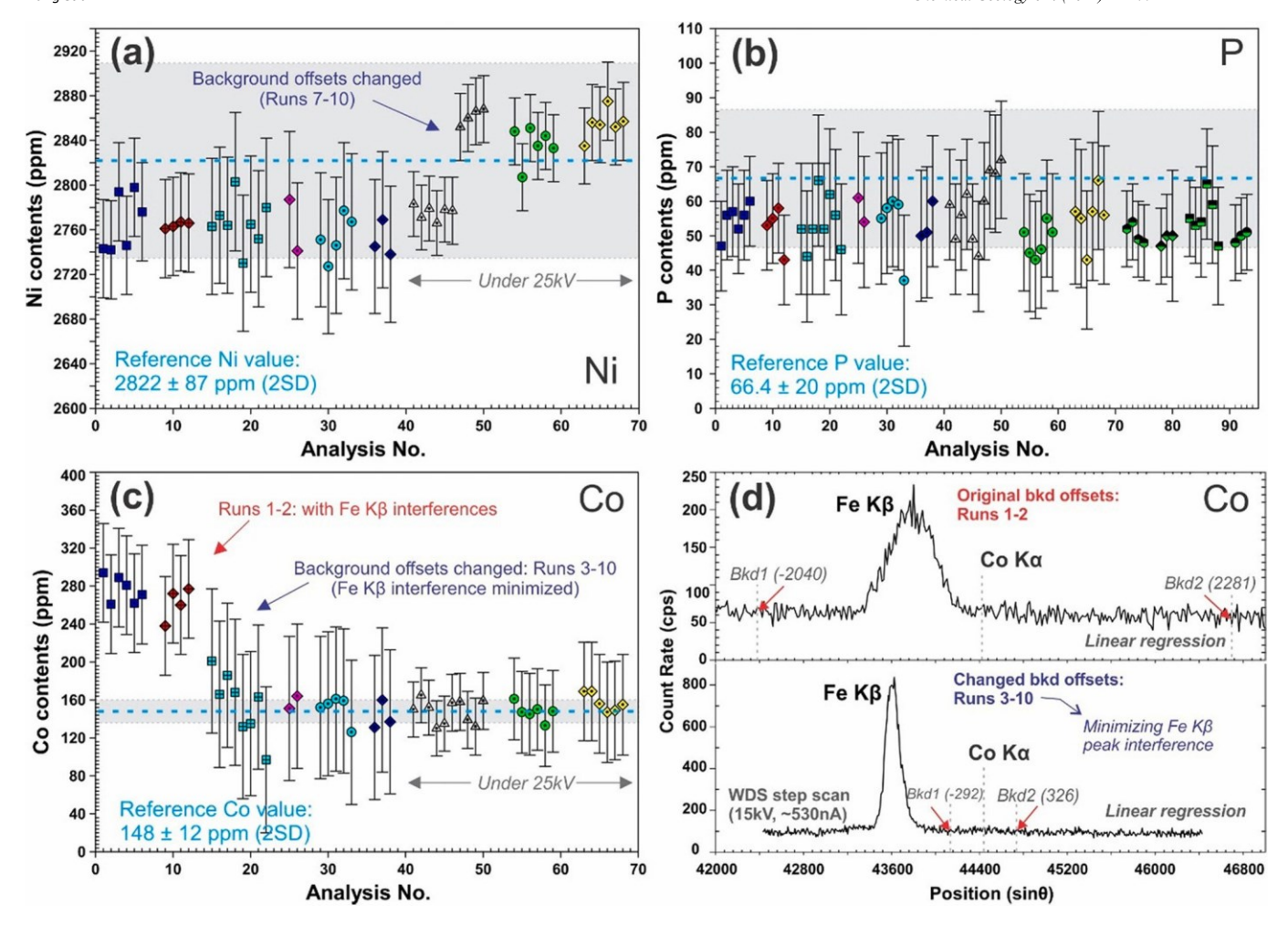


Fig. 9. Accuracy evaluation on elements (Ni, Co, and P) indicative of magmatic differentiation using the MongOlSh11–2 olivine RM. (a) Measured Ni abundances compared to the reference value. Note that a change of background offsets resulted in Ni abundances closer to the reference value. (b) Measured P abundances compared to the reference value. P element analysis yields overall consistent data. (c)-(d) Measured Co abundances compared to the reference value and a sketch illustrating the Fe Kβ interference on Co analysis. It is noted that the Co analysis needs to avoid Fe Kβ interference. Also note that Ni and Co only present 10 runs due to the unstable beam current during Runs 11–14 (see Table S4 for details). For legends in this figure, please refer to Fig. 6.

improved, with the deviation lowered to $^{\sim}6-20\%$ (Fig. 8b), which then rules out the possibility of Zn contamination. These improvements suggest that high voltage can help rapidly increase P/B ratios for low- content elements (e.g., Zn in Suppl. Fig. S1d) and hence improve the accuracy of the analysis, such as Cr (section 5.2) and Zn (Figs. 7f, 8b).

Analysis of Ti via the exponential background regression method yields slightly overestimated values relative to the reference olivine but they are overall consistent within error (Fig. 8c). However, when using the linear background regression method (Run 3), negative Ti contents were obtained (Fig. 8c). The potential WDS spectral "holes" or "negative peaks" both underneath and adjacent the Ti $K\alpha$ peak position (for the LPET crystal) (Donovan et al., 2011) could be one cause for the negative values. But the WDS Ti scan in our study does not show observable "holes" (Fig. 2i), so another likely cause for the negative values is the inaccurate background acquisition. As is shown in Fig. 4d, the detailed WDS step scan of Ti Kα reveals some curvature, where the linear background regression (two-point interpolation) yields significantly overestimated background value at the peak position while the exponential background regression yields more accurate background value. Therefore, the exponential background regression is recommended for EPMA olivine Ti analysis. It should be noted that a "blank" correction can be helpful when artifacts (such as spectral "holes") are present (Donovan et al., 2011; Batanova et al., 2018) and can help improve the data accuracy.

5.4. Indicators of magma differentiation (Ni, Co, and P)

As compatible elements in olivine, Ni and Co are strongly fractionated into olivine during melt crystallization. The greater compatibility of Ni over Co allows Ni/Co ratios to be indicative of magmatic processes.

Wang et al. (2021) claimed that mantle olivines generally have Ni/Co > 20, whereas igneous olivines have gradually decreasing Ni/Co ratios. In particular, olivine forsterite (Fo) — Ni relations are strongly correlated with initial melt composition, crystallization pressures, and extent of fractional crystallization (e.g., Herzberg et al., 2016; Gazel et al., 2018; Gordeychik et al., 2020). Phosphorous is an important element in olivine in that 1) its notable enrichment can indicate rapid olivine growth (rapid cooling), and that 2) its relatively slower diffusion rate makes it a good candidate preserving complicated magmatic processes (mixing, recharge, etc.) and modeling magmatic timescales (e.g., de Maisonneuve et al., 2016; Gordeychik et al., 2018; Shea et al., 2019). In cases where diffusion has not fully erased original element zonation (such as fast- diffusing element Ni), these elements (Ni, Co, and P) can be utilized together to unravel the magmatic processes.

Analysis of Ni yields data consistent with the reference value within uncertainty (Fig. 9a). However, changing background offsets in Runs 7–10 (Table S2.2, Suppl. Fig. S1b) resulted in Ni contents closer to the reference value, with $0.5\% \sim 1.6\%$ deviation, compared to the $2\% \sim 2.2\%$ deviation for Runs 1–6 with original background offsets (Table S4). Therefore, it is recommended to use a wider background offset range for Ni analysis (see Table 2, Suppl. Fig. S1b). Higher voltage under 25 kV also helped notably improve precision of the Ni analysis (Table 2).

Significant improvement in Co accuracy was observed after the background offsets were changed in Runs 3–10 (Fig. 9c-d, Table S2.2). As is shown in Fig. 9d, the Fe K β X-ray peak is very close to Co K α , which can potentially affect Co analysis when using a wide background offset range. A narrow range significantly reduces the Fe K β interference on Co K α analysis (Fig. 9d). In the case where Fe K β interference is notable, an interference correction may be applied. Sobolev et al. (2007) proposed a linear equation to make interference corrections of Fe K β on Co K α : CoOc = CoOm – 0.0011*FeOm – 0.013, where CoOc, CoOm, and FeOm are the corresponding corrected and measured values (wt.%). As noted above with Cr, Mn, Zn and Ni elements, analysis with a higher voltage also greatly improved Co data precision.

Despite the change in background offsets in Runs 3–14, P abundances are consistent with the reference values within errors throughout the 14 runs, revealing only slight underestimation (Fig. 9b). However, Batanova et al. (2019) claimed that phosphorous in MongOlSh11–2 is the only element that shows significant heterogeneity with a homogeneity index of 12. Therefore, the slight underestimation in our study may simply be accounted for by phosphorous heterogeneity. In any case, MongOlSh11–2 olivine can still be a good reference material to monitor P analysis and a correction factor may not be necessary if there is only slight over- or under-estimation of the measured P concentrations.

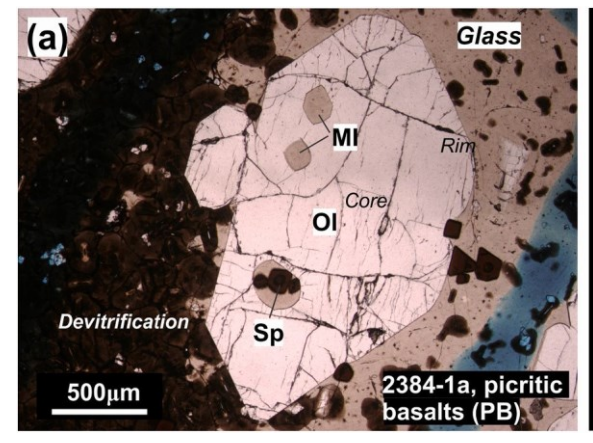
6. Application to olivine samples in the northern East Pacific Rise

With our recommended calibration and quantification settings (Table S1.3; Table 2), we analyzed a few geochemically diverse mid- ocean ridge basalt (MORB) lavas from the Siqueiros Transform and the nearby 8°20′N seamounts adjacent to the EPR. Of particular interest are Siqueiros picritic basalts containing ~10 wt% MgO with up to 20 vol.% olivine phenocrysts (Fig. 10a) that have high forsterite compositions at Fo_{91.5}-Fo_{89.5} (Perfit et al., 1996; Putirka et al., 2011, 2018). Lavas from the 8°20′N seamounts are extremely geochemically heterogeneous (Anderson et al., 2021), including depleted (meaning containing very low concentrations of incompatible elements) MORB (DMORB), normal MORB (NMORB) and a range of highly enriched MORB (EMORB). Olivine in a few representative MORB and picritic basalts were analyzed for their major, minor and trace element compositions (Table 3).

Ca—Ti variations have significant implications for olivine origins (entrapped from the mantle or crystallized from a melt) and history (Foley et al., 2013). Olivines in EMORB in our samples clearly differ from those in DMORB (that

includes picritic basalts, PB), and NMORB by containing lower Ca and higher Ti contents (Fig. 11a). Because both Ca and Ti are incompatible elements in olivine, sole olivine crystallization could lead to Ca and Ti enrichments in the melt and thus the increasing Ca and Ti abundance in olivine, whereas concurrent plagioclase (Ca as a major element, Ti as an incompatible element) crystallization can lower Ca but increase Ti abundances in olivine. Clinopyroxene is rarely observed in the samples, but its crystallization can have similar effect as plagioclase. Therefore, differences in rim compositions (note that all the rim analyses were done at >50 µm from the boundary to minimize the SF effect in particular on Ca element) compared to cores can be explained by the effects of olivine plus or minus plagioclase crystallization on an evolving D- or N- MORB melt, or olivine plus plagioclase plus or minus clinopyroxene crystallization on an EMORB melt (Fig. 11a). Detailed analysis of olivine phenocrysts also reveals complex magmatic histories such as a "depleted" olivine core in an EMORB (4856-12, Fig. 10b) sample that falls just within DMORB "region" (Fig. 11a). As is shown in Fig. 11b, this "depleted" olivine core could be a xenocrystic "mantle" olivine based on the higher Ni/Co ratios (>20) and Ni/Mn ratios (>2) (Wang et al., 2021), whereas the "enriched" olivine rim has a composition reflecting the subsequent evolution of the EMORB melt (i.e., "igneous" overgrowth rim). Therefore, the EMORB sample might record a magmatic history of mantle-melt interaction where mantle olivine residual was entrapped by an enriched melt that ultimately erupted on one of the 8°20′N seamounts. In addition to the mantle olivine cores in the EMORB, many Sigueiros olivines also suggest their "mantle" origin (Fig. 11b). According to Foley et al. (2013), mantle olivines should have restricted Ca-Ti compositions (i.e., Ca < 700 ppm, Ti < 70 ppm). The notable enrichment of Ca (>1800 ppm) of our analyzed mantle olivines (Fig. 11c) can potentially be related with carbonate-silicate melt metasomatism of the original mantle (Foley et al., 2013). Furthermore, we used the mantle lithology tracers, the Mn/Fe – 100*Zn/Fe variations (Fig. 11d), to constrain potential mantle source. It is clear that all the olivine data fall within or around the composition in equilibrium with the peridotite melts, with no direct evidence for a pyroxenite melt source. This suggests that the heterogeneity of the lavas in Siqueiros Transform and the nearby 8°20' N seamounts could partly be correlated with heterogeneous metasomatism of a peridotite mantle.

Our EPR olivine data show that the proposed EPMA analytical protocols in this study can yield accurate data that help discriminate element concentrations at 10s of ppm level (such as Ti, Zn), and help reveal olivine grains of different origin (mantle vs. igneous), constrain



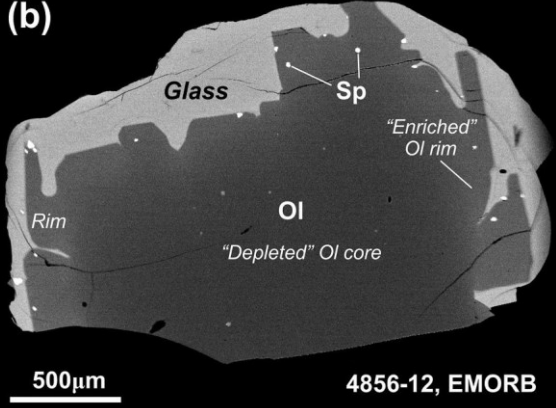


Fig. 10. Optical and BSE images of representative olivine grains from (a) Siqueiros picritic basalts and (b) EMORB from the 8°20′N seamounts. The olivine grains in a picritic basalt (2384-1a) are overall euhedral with no observable embayment. The EMORB sample (4856–12) contains olivine with core-rim BSE zonation. For their geochemical compositions, see Fig. 11. Abbreviations: Ol, olivine; Sp, spinel; MI, melt inclusions.

Table 3
Preliminary EPMA minor and trace element data on 8°20′ N EPR olivine samples.

Corrected EPR data	Weight % (Oxides)			ppm (Element)										Weight %		
Sample info.	MgO SiO2 FeO		Na	Na Al P Ti Cr Mn Co Ni						Ni	Zn	Ca	Oxides Total (wt%)	Fo number (mol%)		
4860-12 01-1, EMORB	43.71	40.64	14.01	72	373	107	157	214	1725	130	1731	74	1715	99.24	84.76	

P. Jiang et al. Chemical Geology 614 (2022) 121199

40CO 12 O1 2 EMODD	44.70	41.61	15.22	cc	262	115	111	460	1700	146	1742	70	1000	102.43	83.96
4860-12_01–2, EMORB	44.70 46.77	41.61	15.22 12.22	66 94	263 431	115 56	144 62	469 425	1798 1449	146 194	1743 2622	79 67	1696 1943	102.43	83.96 87.21
4857-8_03-1, DMORB		42.60					67							102.80	
4857-8_03-2, DMORB	46.07	42.61	12.71	84 51	403 126	86 42	67 47	404	1529 1305	160	2404 1728	85	1991 2036	97.16	86.59 89.27
4847-8_02-1, DMORB	46.61	39.77	9.98		135			360		134		73		97.16	
4847-8_02-2, DMORB	47.12	39.56	10.22	64		42	43	359	1310	137	1778	58	1996		89.15
4847-8_02-3, DMORB	47.40	39.35	10.29	65	130	43	42	406	1283	117	1766	60	1991	97.84	89.14
4856–12_02-c1, EMORB	47.98	40.34	9.34	75	155	34	46	526	1171	146	2808	70	1863	98.59	90.16
4856–12_02-c2, EMORB	47.82	40.74	9.39	62	130	39	42	473	1202	117	2772	74	1860	98.86	90.08
4856–12_02-r1 EMORB	45.41	38.92	12.74	74	94	67	77	229	1653	147	1993	67	1837	97.92	86.40
4856–12_02-r2 EMORB	45.32	38.95	12.87	62	95	63	88	238	1649	115	1972	79	1846	97.98	86.25
OS13-E_01–1, DMORB	46.28	39.39	11.90	57	225	41	46	402	1575	160	2193	65	1969	98.48	87.39
OS13-E_01–2, DMORB	47.59	40.57	12.52	46	197	30	50	370	1544	143	2192	56	2008	101.58	87.14
OS13-E_01–3, DMORB	47.21	40.55	12.18	56	348	84	46	371	1551	122	2214	71	1968	100.88	87.35
4847-7_01-c, DMORB	48.04	41.56	10.90	99	388	67	56	330	1327	141	2105	72	2154	101.42	88.71
4847-7_01-m, DMORB	48.01	41.26	10.88	87	387	27	48	312	1340	142	2085	63	2125	101.05	88.72
4847-7_01-r, DMORB	47.51	41.05	10.69	78	341	8	46	303	1305	135	2098	61	2128	100.13	88.79
4857-8_03-c, DMORB	47.02	40.98	12.00	70	452	97	54	433	1440	157	2737	69	1907	101.02	87.47
4857-8_03-m, DMORB	47.17	41.20	11.81	107	423	92	57	457	1444	143	2711	63	1942	101.20	87.69
4857-8_03-r, DMORB	46.14	40.80	12.75	79	361	78	73	326	1573	160	2289	69	2135	100.67	86.58
OS09-A_02–1, NMORB	46.84	40.73	12.17	66	316	40	60	262	1461	133	2081	72	2097	100.63	87.28
OS09-A_02–2, NMORB	47.04	41.20	12.23	39	288	31	57	330	1465	139	2098	70	2090	101.37	87.27
OS09-A_02-3, NMORB	47.04	41.11	12.23	45	278	25	51	277	1463	161	2110	65	2032	101.27	87.27
2384-1a_01-c, Picritic basalts	49.85	41.38	9.43	73	1826	33	31	344	1149	140	2602	70	2040	101.87	90.40
2384-1a_02-c, Picritic basalts	49.46	41.04	9.44	77	365	31	39	358	1189	151	2668	83	2048	100.90	90.33
2384-1a_01-c, Picritic basalts	47.72	41.12	8.69	74	343	43	42	361	1193	141	2701	78	2138	98.50	90.73
2384-1a_09-c, Picritic basalts	50.27	41.04	8.94	67	371	26	37	473	1098	133	3010	63	2023	101.24	90.93
2384-1a_10-c, Picritic basalts	50.24	41.07	8.81	73	395	46	39	519	1094	132	2991	86	2001	101.13	91.04
2384-1a_11-c, Picritic basalts	48.32	41.02	8.79	81	518	328	44	527	1193	130	3033	80	2110	99.27	90.74
2384-1a_13-c, Picritic basalts	50.24	39.49	9.06	67	392	75	33	421	1061	122	2872	51	2008	99.76	90.81
2384-1a_14-c, Picritic basalts	50.04	41.11	8.78	69	352	77	33	403	1040	164	2936	63	2011	100.90	91.04
2384-1a_04-m, Picritic basalts	47.62	40.90	8.77	79	378	25	48	377	1262	161	2618	74	2194	98.27	90.63
2384-1a_05-m, Picritic basalts	49.37	41.13	9.09	65	401	51	43	386	1258	144	2683	88	2215	100.58	90.64
2384-1a_06-r, Picritic basalts	49.75	41.19	9.24	72	407	34	50	365	1235	133	2690	67	2193	101.17	90.56
2384-1a_06-r, Picritic basalts	49.68	39.65	9.27	59	384	34	49	351	1278	145	2673	80	2210	99.59	90.52
2384-1a_06-r, Picritic basalts	49.64	39.63	9.37	62	355	15	57	344	1201	168	2590	76	2219	99.61	90.43
2384-1a_12-r, Picritic basalts	47.69	40.94	9.16	66	364	24	47	371	1261	143	2676	74	2339	98.79	90.27

Note: 1) Original data were obtained via the PAP matrix correction method. 2) The post-analysis correction of the original data was done by applying a correction factor using the matrix-matched olivine reference material (MongOlSh11–2). Overall, MongOlSh11–2 olivine yields data consistent with reference values, so only minor corrections were made. 3) Some analyses show abnormally high Al (1826 ppm, bolden in text) probably due to presence of spinel inclusion around (or the presence of polishing powder). 4) Some of the totals are above 100 wt% probably due to the non-matrix matched standard calibrations where SiO₂, MgO and FeO were overestimated (due to matrix effect). 5) In the *Sample Info.*, the letters "c", "m", and "r" refer to "core", "mantle", and "rim", repsectively.

detailed magmatic processes and their mantle source lithologies. This method can be applicable to other laboratories that seek to obtain accurate olivine minor and trace elements by EPMA.

7. Conclusions and further implications

The spatial resolution of EPMA olivine analyses can be from <5 μm down to sub-micron scale under 15-25 kV or 10 kV with a focused beam, sufficiently high to analyze complexly grown olivine grains. With less extreme beam conditions (i.e., 15 kV, ~530 nA, 60–120 s peak counting), detection limits for most elements are 10–25 ppm, low enough to analyze trace level elements. As a main focus of the paper, we have systematically evaluated approaches for

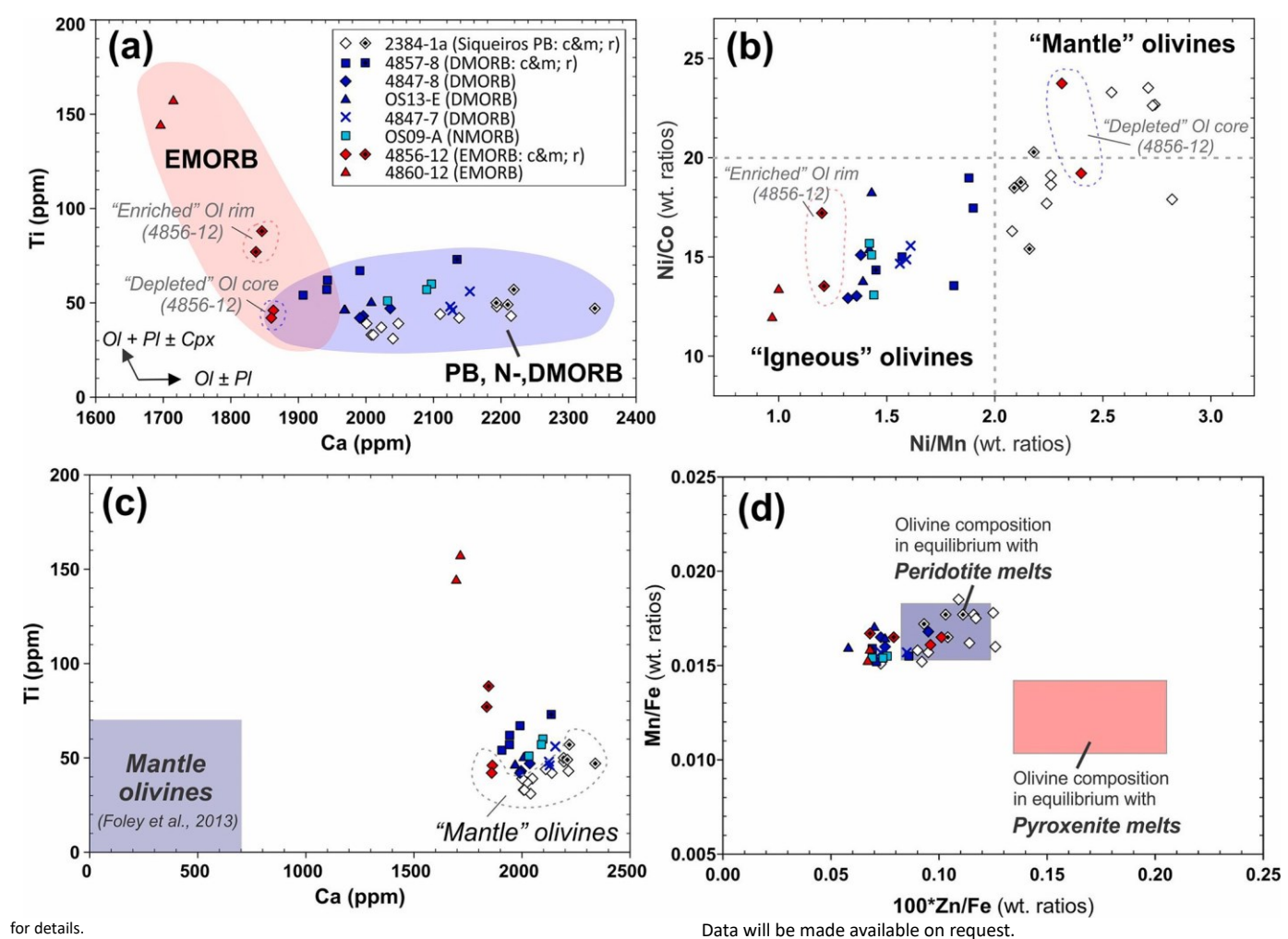
In addition to the beam settings and quantification parameters, specific attention needs to be paid to 1) Na loss by heating; 2) uneven polishing; 3) surface contamination by brass or Al_2O_3 polishing powder; 4) olivine-hosted Cr-Al-rich micro-inclusions such as spinel and chromite; 5) secondary fluorescence from adjacent phases containing large abundances of the elements of interest. In order to acquire accurate Na concentrations, it needs to be the first element to analyze in one single analysis to avoid significant Na loss. Fine-polishing and ultrasonic cleaning in intermediate steps and plasma cleaning immediately prior to EPMA experiments are recommended to avoid any Zn and Al contaminations. Careful microscopic observations need to be made to avoid compromised Cr and Al signals from the spinel and chromite inclusions in olivine, as well as the effects of their secondary fluorescence X-rays. In

Fig. 11. Geochemical plots for EPR olivine data obtained by our proposed EPMA analytical protocols. (a) Ca–Ti variations of olivines from Siqueiros picritic basalts (PB), and 8°20′N seamounts DMORB, NMORB, and EMORB. While PB, D- and N-MORB olivines are characterized by lower Ti and higher Ca, the EMORB olivines show lower Ca and higher Ti. The cores and mantles ("c&m") and rims ("r") depict fractional crystallization trends (olivine, plagioclase and clinopyroxene). (b) Ni/ Co-Ni/Mn variations indicative of mantle and igneous olivines. Siqueiros PB olivines are basically of "mantle" origin, with rims or some grains showing melt-mantle interaction (which lowered the Ni/Co ratios below 20). The olivine cores from the 44856-12 sample (Fig. 10b) also show mantle origin. (c) A rescaled Ca–Ti variations of EPR olivine data in comparison with mantle olivine compositions defined by Foley et al. (2013). The notable Ca enrichment of the mantle olivines in this study can be observed. (d) Mn/Fe-100*Zn/Fe variations of olivines. All data fall within the olivine composition in equilibrium with peridotite melts. See Section 6

accurate EPMA olivine analyses. Among all the beam settings, high voltage, high beam current and long counting time not only improve data precision, but also improve data accuracy, especially on those elements with low P/B ratios such as Zn and Cr. In comparison, beam size changes do not have effect on either precision or accuracy of the data, which gives more confidence for high spatial resolution analysis (with a focused beam). Background offset changes on Na, Ca, Mn, and P do not have notable effects on data accuracy, but significant effects are observed on Ni and Co, where a wider background offset range is recommended for Ni and a narrow range free of Fe K β peak interference is needed for Co. Regarding background regression models, except for Mn, Al, and Ti, where exponential regression is required, all other elements can apply linear regression models.

particular, the Ca analysis in olivine needs to consider the SF effect from adjacent Ca-rich phases (such as plagioclase, pyroxene, and glass).

Our systematic tests and evaluations indicate that MongOlSh11–2 olivine is overall a very good primary matrix-matched olivine standard for major elements (Mg, Fe, Si) calibrations and a reference material for minor and trace element data accuracy monitoring. Slight Na, Ca, and P heterogeneity may be present in MongOlSh11–2 olivine RM, where



researchers are advised to focus their analyses on a small restricted area to minimize the heterogeneity effect. Due to instrumental differences among laboratories, systematic underestimation or overestimation may occur, to which an appropriate correction factor can be applied.

While precautions and protocols can be applied, it is always appropriate to set specific settings for specific application cases. For example, if Al-in-olivine thermometer is the focus of a study, multiple spectrometers can be counted simultaneously, along with high beam current, voltage, and long counting time, to increase the precision (e.g., Jennings et al., 2019; Goltz et al., 2020). However, EPMA has its limitations in accurately measuring elements <5–10 ppm (such as Li, Sc, V, Cu), or below 1 ppm (such as Sr, Y, Zr and REEs). In cases where olivine growth zones are large (>50-100 μ m), or the grains are homogenous, LA-ICP-MS method can be applied to obtain these elements with extremely low concentrations. It is expected that combined EPMA and LA-ICP-MS (and potentially SIMS) techniques can be applied to fully unravel detailed olivine growth history. As a full set of minor and trace elements are analyzed, with sufficient high precision and accuracy, olivine data can be confidently compared from different case studies to form a big database, which benefit researchers worldwide.

Declaration of Competing Interest

The authors declare that they have no known competing financial interests or personal relationships that could have appeared to influence the work reported in this paper.

Data availability

Acknowledgement

Special thanks are given to Dr. Valentina G. Batanova from University Grenoble Alpes who provided us the international MongOlSh11-2 olivine reference material. We also thank Drs. Brent Gila and Amelia Dempere for granting the EPMA development work on olivine. We greatly appreciate the editorial handling of this manuscript by Editor-in- Chief Dr. Balz Kamber. Dr. Teresa Ubide and one anonymous reviewer are thanked for their insightful comments and suggestions that have helped greatly improve the quality of this manuscript. The EPMA at the University of Florida (UF) was funded by a grant from the National Science Foundation (NSF) (DMR1429265). This method development work was partially supported by NSF OCE-MGG 1357150 (Perfit) and the UF Research Opportunity Fund (Foster and Perfit). Analysis of EPR olivine samples was supported by NSF grant OCE2001314 (Perfit).

Appendix A. Supplementary data

Supplementary data to this article can be found online at https://doi.org/10.1016/j.chemgeo.2022.121199.

References

Anderson, M., Wanless, V.D., Perfit, M., Conrad, E., Gregg, P., Fornari, D., Ridley, W.I., 2021. Extreme heterogeneity in mid-ocean ridge mantle revealed in lavas from the 8'20'N near-axis seamount chain. Geochem. Geophys. Geosyst. 22, 1–22. https://doi.org/10.1029/2020GC009322.

Batanova, V.G., Sobolev, A.V., Kuzmin, D.V., 2015. Trace element analysis of olivine: high precision analytical method for JEOL JXA-8230 electron probe microanalyser.

Chem. Geol. 419, 149–157. https://doi.org/10.1016/j.chemgeo.2015.10.042.

- Batanova, V.G., Sobolev, A.V., Magnin, V., 2018. Trace element analysis by EPMA in geosciences: detection limit, precision and accuracy. IOP Conf. Ser. Mater. Sci. Eng. 304, 0–17. https://doi.org/10.1088/1757-899X/304/1/012001.
- Batanova, V.G., Thompson, J.M., Danyushevsky, L.V., Portnyagin, M.V., Garbe- Schonberg, D., Hauri, E., Kimura, J.I., Chang, Q., Senda, R., Goemann, K., "Chauvel, C., Campillo, S., Ionov, D.A., Sobolev, A.V., 2019. New olivine reference material for in situ microanalysis. Geostand. Geoanal. Res. 43. 453–473. https://doi.org/10.1111/ggr.12266.
- Bussweiler, Y., Giuliani, A., Greig, A., Kjarsgaard, B.A., Petts, D., Jackson, S.E., Barrett, N., Luo, Y., Pearson, D.G., 2019. Trace element analysis of high-Mg olivine by LA-ICP-MS Characterization of natural olivine standards for matrix-matched calibration and application to mantle peridotites. Chem. Geol. 524, 136–157. https://doi.org/10.1016/i.chemgeo.2019.06.019.
- Coogan, L.A., Saunders, A.D., Wilson, R.N., 2014. Aluminum-in-olivine thermometry of primitive basalts: Evidence of an anomalously hot mantle source for large igneous provinces. Chem. Geol. 368, 1–10. https://doi.org/10.1016/j. chemgeo.2014.01.004.
- Costa, F., Shea, T., Ubide, T., 2020. Diffusion chronometry and the timescales of magmatic processes. Nat. Rev. Earth Environ. 1, 201–214. https://doi.org/10.1038/s43017-020-0038-
- Dalton, J.A., Lane, S.J., 1996. Electron microprobe analysis of Ca in olivine close to grain boundaries: the problem of secondary X-ray fluorescence. Am. Mineral. 81, 194–201. https://doi.org/10.2138/am-1996-1-224.
- De Hoog, J.C.M., Gall, L., Cornell, D.H., 2010. Trace-element geochemistry of mantle olivine and application to mantle petrogenesis and geothermobarometry. Chem.
- Geol. 270, 196–215. https://doi.org/10.1016/j.chemgeo.2009.11.017. de Maisonneuve, C.B., Costa, F., Huber, C., Vonlanthen, P., Bachmann, O., Dungan, M.A., 2016. How do olivines record magmatic events? Insights from major and trace element zoning. Contrib. Mineral. Petrol. 171, 1–20. https://doi.org/10.1007/s00410-016-1264-6.
- Donovan, J.J., Lowers, H.A., Rusk, B.G., 2011. Improved electron probe microanalysis of trace elements in quartz. Am. Mineral. 96, 274–282. https://doi.org/10.2138/am.2011.3631.
- Drouin, D., Couture, A.R., Joly, D., Tastet, X., Aimez, V., Gauvin, R., 2007. CASINO V2.42 A fast and easy-to-use modeling tool for scanning electron microscopy and microanalysis users. Scanning 29, 92–101. https://doi.org/10.1002/sca.20000.
- Foley, S.F., Prelevic, D., Rehfeldt, T., Jacob, D.E., 2013. Minor and trace elements in olivines as probes into early igneous and mantle melting processes. Earth Planet. Sci. Lett. 363, 181–191. https://doi.org/10.1016/j.epsl.2012.11.025.
- Gavrilenko, M., Herzberg, C., Vidito, C., Carr, M.J., Tenner, T., Ozerov, A., 2016. A calcium-inolivine geohygrometer and its application to subduction zone magmatism. J. Petrol. 57, 1811–1832. https://doi.org/10.1093/petrology/egw062.
- Gazel, E., Trela, J., Bizimis, M., Sobolev, A., Batanova, V., Class, C., Jicha, B., 2018. Long- lived source heterogeneities in the galapagos mantle plume. Geochem. Geophys. Geosyst. 19, 2764–2779. https://doi.org/10.1029/2017GC007338.
- Goltz, A.E., Krawczynski, M.J., Gavrilenko, M., Gorbach, N.V., Ruprecht, P., 2020. Evidence for superhydrous primitive arc magmas from mafic enclaves at Shiveluch volcano, Kamchatka. Contrib. Mineral. Petrol. 175, 1–26. https://doi.org/10.1007/s00410-020-01746-5.
- Gomez-Ulla, A., Sigmarsson, O., Gudfinnsson, G.H., 2017. Trace element systematics of 'olivine from historical eruptions of Lanzarote, Canary Islands: Constraints on mantle source and melting mode. Chem. Geol. 449, 99–111. https://doi.org/10.1016/j. chemgeo.2016.11.021.
- Gordeychik, B., Churikova, T., Kronz, A., Sundermeyer, C., Simakin, A., Worner, G., "
 2018. Growth of, and diffusion in, olivine in ultra-fast ascending basalt magmas from
 Shiveluch volcano OPEN. Sci. Rep. 8, 11775. https://doi.org/10.1038/s41598-018-30133-1.
- Gordeychik, B., Churikova, T., Shea, T., Kronz, A., Simakin, A., Worner, G., 2020. Fo and "Ni relations in olivine differentiate between crystallization and diffusion trends. J. Petrol. 61, 1–23. https://doi.org/10.1093/petrology/egaa083.
- Hazarika, P., Mishra, B., Ozha, M.K., Pruseth, K.L., 2017. An improved EPMA analytical protocol for U-Th-Pbtotal dating in xenotime: age constraints from polygenetic Mangalwar Complex, Northwestern India. Chem. Erde 77, 69–79. https://doi.org/10.1016/j.chemer.2017.01.010.
- Herzberg, C., Vidito, C., Starkey, N.A., 2016. Nickel-cobalt contents of olivine record origins of mantle peridotite and related rocks. Am. Mineral. 101, 1952–1966. https://doi.org/10.2138/am-2016-5538.
- Howarth, G.H., Harris, C., 2017. Discriminating between pyroxenite and peridotite sources for continental flood basalts (CFB) in southern Africa using olivine chemistry. Earth Planet. Sci. Lett. 475, 143–151. https://doi.org/10.1016/j. epsl.2017.07.043.
- Hrushikesh, H., Singh, P.C., Prabhakar, N., Thakur, S.K., Dey, B., 2020. Tectonothermal evolution of a collisional orogen in the Khammam region, southeastern India: insights from structures, phase equilibria modeling and U-Th-(total) Pb monazite geochronology. Contrib. Mineral. Petrol. 175, 1–20. https://doi.org/10.1007/s00410-020-01744-7.
- Jankovics, M.E., S agi, T., Astbury, R.L., Petrelli, M., Kiss, B., Ubide, T., N´ ´emeth, K., Ntaflos, T., Harangi, S., 2019. Olivine major and trace element compositions coupled with spinel chemistry to unravel the magmatic systems feeding monogenetic basaltic volcanoes.
 J. Volcanol. Geotherm. Res. 369, 203–223. https://doi.org/10.1016/j.ivolgeores.2018.11.027.
- Jennings, E.S., Gibson, S.A., Maclennan, J., 2019. Hot primary melts and mantle source for the Parana-Etendeka flood basalt province: New constraints from Al-in-olivine 'thermometry. Chem. Geol. 529, 119287 https://doi.org/10.1016/j. chemgeo.2019.119287.
- Jercinovic, M.J., Williams, M.L., Lane, E.D., 2008. In-situ trace element analysis of monazite and other fine-grained accessory minerals by EPMA. Chem. Geol. 254, 197–215. https://doi.org/10.1016/j.chemgeo.2008.05.016.
- Jercinovic, M.J., Williams, M.L., Allaz, J., Donovan, J.J., 2012. Trace analysis in EPMA. IOP Conf. Ser. Mater. Sci. Eng. 32, 0–22. https://doi.org/10.1088/1757-899X/32/1/012012.

- Johnson, C., Crispin, K.L., Yablon, D., 2019. Probing sample preparation as a pathway to analysis improvement. In: QMA 2019 Program Guide with Abstract, pp. 16–17.
- Kone cný, P., Kusiak, M.A., Dunkley, D.J., 2018. Improving U-Th-Pb electron microprobe dating using monazite age references. Chem. Geol. 484, 22–35. https://doi.org/ 10.1016/j.chemgeo.2018.02.014.
- Le Roux, V., Dasgupta, R., Lee, C.T.A., 2011. Mineralogical heterogeneities in the Earth's mantle: constraints from Mn, Co, Ni and Zn partitioning during partial melting. Earth Planet. Sci. Lett. 307, 395–408. https://doi.org/10.1016/j.epsl.2011.05.014.
- Li, J., Huang, X.L., Li, X.H., Chu, F.Y., Zhu, J.H., Zhu, Z.M., Wang, H., 2021. Anomalously hot mantle source beneath the Dragon Flag Supersegment of the Southwest Indian Ridge: new evidence from crystallisation temperatures of mid-ocean ridge basalts. Lithos 396–397, 106221. https://doi.org/10.1016/j.lithos.2021.106221.
- Liu, Z., Shea, J.J., Foley, S.F., Bussweiler, Y., Rohrbach, A., Klemme, S., Berndt, J., 2021. Clarifying source assemblages and metasomatic agents for basaltic rocks in eastern Australia using olivine phenocryst compositions. Lithos 390–391, 106122. https://doi.org/10.1016/i.lithos.2021.106122.
- Llovet, X., Galan, G., 2003. Correction of secondary X-ray fluorescence near grain boundaries in electron microprobe analysis: application to thermobarometry of spinel lherzolites. Am. Mineral. 88, 121–130. https://doi.org/10.2138/am-2003-0115.
- Llovet, X., Salvat, F., 2016. PENEPMA: A Monte Carlo programme for the simulation of X-ray emission in EPMA. IOP Conf. Ser. Mater. Sci. Eng. 109 https://doi.org/ 10.1088/1757-899X/109/1/012009.
- Llovet, X., Proenza, J.A., Pujol-Sola, N., Farr` 'e-De-Pablo, J., Campeny, M., 2020 Correction of secondary fluorescence across phase boundaries in electron probe microanalysis of mineral inclusions. Microsc. Microanal. 26, 895–905. https://doi. org/10.1017/51431927620024393.
- Llovet, X., Moy, A., Pinard, P.T., Fournelle, J.H., 2021. Electron probe microanalysis: a review of recent developments and applications in materials science and engineering. Prog. Mater. Sci. 116, 100673 https://doi.org/10.1016/j.pmatsci.2020.100673.
- Merlet, C., 1992. Quantitative electron probe microanalysis: new accurate Φ (pz) description. Microchim. Acta 107–115. https://doi.org/10.1007/978-3-7091-6679- 6_8 [Suppl.].
- Merlet, C., 1994. An accurate computer correction program for quantitative electron probe microanalysis. Mikrochim. Acta 114 (115), 363–376.
- Neave, D.A., Shorttle, O., Oeser, M., Weyer, S., Kobayashi, K., 2018. Mantle-derived trace element variability in olivines and their melt inclusions. Earth Planet. Sci. Lett. 483, 90–104. https://doi.org/10.1016/j.epsl.2017.12.014.
- Nekrylov, N., Plechov, P.Y., Gritsenko, Y.D., Portnyagin, M.V., Shcherbakov, V.D., Aydov, V.A., Garbe-Schonberg, D., 2021. Major and trace element composition of "olivine from magnesian skarns and silicate marbles. Am. Mineral. 106, 206–215. https://doi.org/10.2138/am-2020-7566.
- Newbury, D.E., 2002. Microanalysis for low voltage scanning electron microscopy. J. Res. Natl. Inst. Stand. Technol. 107. 605–619.
- Perfit, M.R., Fornari, D.J., Ridley, W.I., Kirk, P.D., Casey, J., Kastens, K.A., Reynolds, J. R., Edwards, M., Desonie, D., Shuster, R., Paradis, S., 1996. Recent volcanism in the Siqueiros transform fault: Picritic basalts and implications for MORB magma genesis. Earth Planet. Sci. Lett. 141, 91–108. https://doi.org/10.1016/0012-821x/96100052-0.
- Pouchou, J.-L., Pichoir, F., 1991. Quantitative analysis of homogeneous or stratified microvolumes applying the model "PAP". Electron Probe Quant. 31–75 https://doi. org/10.1007/978-1-4899-2617-3 4.
- Putirka, K., Ryerson, F.J., Perfit, M., Ridley, W.I., 2011. Mineralogy and composition of the oceanic mantle. J. Petrol. 52, 279–313. https://doi.org/10.1093/petrology/egq080.
- Putirka, K., Tao, Y., Hari, K.R., Perfit, M.R., Jackson, M.G., Arevalo, R., 2018. The mantle source of thermal plumes: Trace and minor elements in olivine and major oxides of primitive liquids (and why the olivine compositions don't matter). Am. Mineral. 103, 1253–1270. https://doi.org/10.2138/am-2018-6192.
- Rasmussen, M.B., Halldorsson, S.A., Gibson, S.A., Guðfinnsson, G.H., 2020. Olivine ´ chemistry reveals compositional source heterogeneities within a tilted mantle plume beneath Iceland. Earth Planet. Sci. Lett. 531, 116008 https://doi.org/10.1016/j.epsl.2019.116008.
- Sanfilippo, A., Tribuzio, R., Tiepolo, M., 2014. Mantle-crust interactions in the oceanic lithosphere: Constraints from minor and trace elements in olivine. Geochim. Cosmochim. Acta 141, 423–439. https://doi.org/10.1016/j.gca.2014.06.012.
- Shaikh, A.M., Patel, S.C., Bussweiler, Y., Kumar, S.P., Tappe, S., Ravi, S., Mainkar, D., 2019. Olivine trace element compositions in diamondiferous lamproites from India: Proxies for magma origins and the nature of the lithospheric mantle beneath the Bastar and Dharwar cratons. Lithos 324–325, 501–518. https://doi.org/10.1016/j. lithos.2018.11.026.
- Shea, T., Hammer, J.E., Hellebrand, E., Mourey, A.J., Costa, F., First, E.C., Lynn, K.J., Melnik, O., 2019. Phosphorus and aluminum zoning in olivine: contrasting behavior of two nominally incompatible trace elements. Contrib. Mineral. Petrol. 174, 1–24. https://doi.org/10.1007/s00410-019-1618-y.
- Shi, J.-H., Zeng, G., Chen, L.-H., Hanyu, T., Wang, X.-J., Zhong, Y., Xie, L.-W., Xie, W.-L., 2022. An eclogitic component in the Pitcairn mantle plume: evidence from olivine compositions and Fe isotopes of basalts. Geochim. Cosmochim. Acta 318, 415–427. https://doi.org/10.1016/j.gca.2021.12.017.
- Sobolev, A.V., Hofmann, A.W., Kuzmin, D.V., Yaxley, G.M., Arndt, N.T., Chung, S.-L., Danyushevsky, L.V., Elliott, T., Frey, F.A., Garcia, M.O., Gurenko, A.A.,
 - Kamenetsky, V.S., Kerr, A.C., Krivolutskaya, N.A., Matvienkov, V.V., Nikogosian, I. K., Rocholl, A., Sigurdsson, I.A., Sushchevskaya, N.M., Teklay, M., 2007. The amount of recycled crust in sources of mantle-derived melts. Science (80-.) 316, 412–418. https://doi.org/10.1126/science.1138113.

- Su, B., Chen, Y., Mao, Q., Zhang, D., Jia, L.H., Guo, S., 2019. Minor elements in olivine inspect the petrogenesis of orogenic peridotites. Lithos 344–345, 207–216. https://doi.org/10.1016/j.lithos.2019.06.029.
- Trela, J., Gazel, E., Sobolev, A.V., Moore, L., Bizimis, M., Jicha, B., Batanova, V.G., 2017.

 The hottest lavas of the Phanerozoic and the survival of deep Archaean reservoirs.

 Nat. Geosci. 10, 451–456. https://doi.org/10.1038/ngeo2954.
- Wan, Z., Coogan, L.A., Canil, D., 2008. Experimental calibration of aluminum partitioning between olivine and spinel as a geothermometer. Am. Mineral. 93, 1142–1147. https://doi.org/10.2138/am.2008.2758.
- Wang, J., Su, B.X., Robinson, P.T., Xiao, Y., Bai, Y., Liu, X., Sakyi, P.A., Jing, J.J., Chen, C., Liang, Z., Bao, Z.A., 2021. Trace elements in olivine: Proxies for petrogenesis, mineralization and discrimination of mafic-ultramafic rocks. Lithos 388–389, 106085. https://doi.org/10.1016/j.lithos.2021.106085.
- Williams, M.L., Jercinovic, M.J., Mahan, K.H., Dumond, G., 2017. Electron microprobe petrochronology. Rev. Mineral. Geochem. 83, 153–182. https://doi.org/10.2138/ rmg.2017.83.5.
- Yang, F., Huang, X.L., Xu, Y.G., He, P.L., 2021. Cryptic zoning in primitive olivine as an archive of mush fluidization at mid-ocean ridges. Lithos 390–391, 106121. https://doi.org/10.1016/j.lithos.2021.106121.
- Zhang, D., Su, B., Chen, Y., Yang, W., Mao, Q., Jia, L.H., 2022. Titanium in olivine reveals low-Ti origin of the Chang'E-5 lunar basalts. Lithos 414–415. https://doi.org/10.1016/j.lithos.2022.106639.